学位申請論文

藤沢　博

A cw 4-rod RFQ Linac

Hiroshi Fujisawa

R&D Division, Nissin Electric Co., Ltd.
575 Kuze Tonoshiro-cho, Minami-ku, Kyoto-shi, Kyoto-fu 601 Japan
and
Accelerator Laboratory
Institute for Chemical Research, Kyoto University
Gokanosho, Uji-shi, Kyoto-fu 611 Japan

Abstract

A cw 4-rod RFQ linac system has been designed, constructed, and tested as an accelerator section of a MeV-class ion implanter system. The tank diameter is only 60 cm for 34 MHz operating frequency. An equally-spaced arrangement of the RFQ electrode supporting plates is proved to be suitable for a low resonant frequency 4-rod RFQ structure. The RFQ electrode cross section is not circular but rectangular to make the handling and maintenance of the electrodes easier. The machining of the electrode is done three dimensionally. Second order corrections in the analyzing magnet of the LEBT (Low Energy Beam Transport) section assure a better transmission through and the matching to the RFQ. A new approach is introduced to measure the rf characteristics of the 4-rod RFQ. This method requires only a few capacitors and a network analyzer. Both the rf and thermal stability of the 4-rod RFQ are tested up to cw 50 kW. Beam experiments with several ions confirm the acceleration of beams to the goal energy of 83 keV/u. The ion beam intensities obtained at the RFQ output for He^+, N^{2+}, and C^+ are 32, 13, and 220 pμA, respectively. The measured beam transmissions of ≥ 80 % agree with the PARMTEQ calculations. The ion implantation method also gives definitive information on the energies of an RFQ output beam.

1. Introduction

The applications of MeV ion implantation have been known for almost 10 years. Several important review articles on the subject have been published [1-4]. In those articles, the nature of high energy implants, proposed applications, available production machines, and the problems associated with this new technology were discussed with references. From 1986 to 1987, there were reports from equipment manufactures about design of versatile commercial MeV ion implanters [5-7]. It was the first time that rf accelerators, particularly RFQ's, were recognized as candidates of high current and high energy ion accelerators in industrial applications. This recognition of RFQ came 16 years after the invention of the RFQ principle by Kapchinskii and Teplyakov [8] and 6 years after a successful proof of the RFQ principle at Los Alamos Scientific Laboratory [9]. Since then, both the developments of rf-accelerator-based implanters and the industrial applications of MeV implantation have grown fast. Good reviews of the applications of accelerators are found in ref. [10,11] and many practical utilizations of this technology have been reported from several research laboratories [12-17].

The RFQ linacs are suitable for industrial use because of their small sizes and easier X-ray shielding requirements. A rod-type structure has been selected in our case because the diameter of the RFQ cavity has become smaller. The design and tuning of this type of RFQ are expected to be much simpler than vane-type RFQs. We adopted the "linear $\lambda/2$-RFQ" structure that was originally proposed in 1985 by a group of Frankfurt University [18-19]. An independent work on the 4-rod structure was started in 1986 in collaboration between Nissin Electric Co., Ltd. and The Accelerator Laboratory of The Institute of Chemical Research (ICR), Kyoto University [20]. Our first objective was to construct a small 100 MHz proton model and to get a feeling for how the building a commercial ion RFQ linac could be approached. Our reports on the 100 MHz 4-rod RFQ are found in ref. [21-24]. Design work on a heavy ion RFQ was started soon after the

completion of the proton accelerator model [25-26] and the joint research project between Nissin and ICR has been continuing to date.

The outline of this paper is as follows: Section 2 illustrates the overall design and the specifications of our RFQ linac system. Section 3 describes the RFQ electrode parameters and the results of the RFQ beam dynamics studies. Section 4 deals with the mechanical design of the RFQ electrode assembly and its cavity. Section 5 details the design and construction of the ion injection system with emphasis on low energy ion optics. Section 6 is concerned with the rf power amplifier system. Section 7 gives the architecture of the linac control system. Section 8 and 9 present the rf tests of the 4-rod RFQ at low and high power operation, respectively. Section 10 explains the beam acceleration experiments. Section 11 gives conclusion and discussion.

2. General considerations

There are some important points to be considered in designing a cw 4-rod RFQ linac. The following is a list of general criterion that the author has considered important for designing our RFQ linac:

1. Length of RFQ cavity is around 2 m.
2. Diameter of RFQ cavity is less than 90 cm.
3. Power efficiency.
4. Beam transmission.
5. Thermal stability.
6. rf contact.
7. Local heating by rf.
8. rf protection of o-rings.
9. No rf or X-rays leak to the outside cavity.
10. Vacuum condition 5.0×10^{-7} Torr (rf off) and 1.0×10^{-6} Torr (rf on).
11. Maintenance and accessibility.
12. Cost and performances.

Table 1 gives the specifications of our 4-rod RFQ based on the above considerations.

Included in the ion injector to the RFQ is a Freeman type ion source designed for commercial uses. The stability and reliability of the ion source have been proven in various industrial environments. The 90 degree mass analyzer filters out unnecessary components of the extracted beam, thereby protecting the RFQ electrode from being spattered by those particles. The magnetic quadrupoles and an Einzel lens match the beam to the RFQ. The beam quality is preserved through out the beam transport line by including the sextupole corrections in the mass analyzer. All the components in the ion injector are arranged in a compact X-ray-shielded cabinet.

The RFQ is of fixed-frequency "modified" 4-rod type. The resonant frequency is 33.3 MHz, which is lower by one order of magnitude compared with the most of existing light ion RFQs. The lower operating frequency is preferred for the acceleration of heavy ions. The size of the RFQ cavity is shrunk to one of the smallest in this operating frequency. To get higher average beam current, which is preferable in many applications, the RFQ operates in cw mode.

The RFQ should be able to accelerate a single charge oxygen beam—charge to mass ratio of 1/16—up to MeV energies. B^+ and P^{2+} ions—most used ion species in the present application of MeV implantation—can then be accelerated as well in the RFQ. The beam transmission of 80 % or better and nominal average output beam current of 200 μA should fulfill most of the current user requirements.

3. RFQ Electrode

3.1. Electrode parameter optimization OPTIMIZER runs

The two lowest-order terms potential function of the RFQ given by Kapchinskii and Teplyakov is written in cylindrical coordinates as follows [8] :

$$U(r,\psi,z)=\frac{V}{2}\left(X\left(\frac{r}{a}\right)^2\cos 2\psi + AI_0(kr)\cos kz\right)\cdot\sin(\omega t+\phi), \qquad (1)$$

where V is the potential difference between adjacent pole tips, a is the minimum displacement of the RFQ electrode from the z axis (minimum aperture radius), I_0 is the modified Bessel function of order zero, ω is the rf frequency, and ϕ is the rf phase. The other quantities in eq. (1) are defined:

$$k=\frac{\pi}{L}, \qquad (2)$$

where $L = \beta\lambda/2$ is the length of one "cell" of the RFQ, β is the velocity of particle/c, λ is rf wavelength,

$$A=\frac{m^2-1}{m^2I_0(ka) + I_0(mka)}, \qquad (3)$$

where m is the RFQ electrode modulation parameter, and

$$X = 1 - AI_0(ka). \qquad (4)$$

From eq. (1) the following electric field components are obtained:

$$E_r=-\left(\frac{XV}{a^2}r\cos 2\psi+\frac{kAV}{2}I_1(kr)\cos kz\right)\cdot\sin(\omega t+\phi), \qquad (5)$$

where I_1 is the modified Bessel function of order one,

$$E_\psi=\frac{XV}{a^2}r\sin 2\psi\cdot\sin(\omega t+\phi), \qquad (6)$$

$$E_z=\frac{kAV}{2}I_0(kr)\sin kz\cdot\sin(\omega t+\phi). \qquad (7)$$

The quantity AV is the potential difference that exists on the z axis between the beginning and the end of the unit cell:

$$U(0,0,0) - U(0,0,L) = AV \tag{8}$$

The space-average longitudinal field E_0 is given by:

$$E_0 = \frac{\int_0^{\beta\lambda/2} E_z \, dz}{\beta\lambda/2} = \frac{2AV}{\beta\lambda}. \tag{9}$$

The energy gain ΔE of a particle with charge q and synchronous velocity βc in a unit cell length L is then given:

$$\frac{\Delta E}{L} = qE_0 T \cos\phi_s, \tag{10}$$

where $T=\pi/4$ is the transit-time factor and ϕ_s is the rf synchronous phase at the beginning of the cell. The quantity A is then called acceleration efficiency parameter. The first term in eq. (5) and eq. (6) gives electric quadrupole field with the strength of XV/a^2 Thereby X is called focusing force parameter.

The two other important parameters that pertain to the radial stability of particle motions are focusing parameter B and rf defocusing parameter Δ_{rf}:

$$B = \frac{q\lambda^2}{Mc^2} \cdot \frac{XV}{a^2}, \tag{11}$$

$$\Delta_{rf} = \frac{\pi^2 qVA \sin\phi}{2Mc^2\beta^2}, \tag{12}$$

where M is the rest mass of the particle. The foundation of designing an RFQ lies in searching the appropriate values of those RFQ parameters for a particular application that the RFQ is to be used.

The RFQ electrode parameters were determined using an optimization program called OPTIMIZER written in *Mathematica®*

[27]. The principle is similar to the one developed at INS, University of Tokyo for the optimization of heavy ion RFQ linac [28-30]. OPTIMIZER is basically an aid tool that helps find the optimum electrode parameters of an RFQ, where optimum means short electrode length with reasonable beam transmission. There are four categories of input variables to be specified in the program such as the input and output beam parameters, the number of cells in the six sections of the RFQ, final values of the electrode parameters and the functional dependence of the electrode parameters in each section. One can work interactively on the program viewing the results graphically on the computer screen. The program also makes a file to be read in PARMTEQ code [31]. Fig. 1 shows the result of RFQ electrode parameters obtained in an OPTIMIZER run and the key RFQ parameters are listed in table 2.

The average bore radius of the RFQ is set to 8 mm, which is about twice as large as most existing RFQs. This relaxes the machining and assembling tolerances so that the cost of electrodes can be kept considerably low. The transverse acceptance of the RFQ becomes larger because it is proportional to the square of the aperture radius [32-33]. Reasonably good beam transmission is also sought with a moderate value of the inter-electrode voltage. This is especially important in obtaining an rf-efficient cw-machine. The design value of inter-electrode voltage is 54.9 kV which corresponds to approximately 1.3 times of Kilpatrick limit, with a field enhancement factor of 1.5 [33-35].

3.2. Beam dynamics calculation PARMTEQ runs

Beam dynamics calculations have been done using a PARMTEQ code. The modifications to the code were made so that beam dynamics calculations can be done independently with the generation of RFQ linac parameters. This means for example that one can simulate the dynamics of a C^+ ion beam of any injection energies in the RFQ linac which parameters are generated for a B^+ ion beam at certain injection energy. Fig. 2 shows the beam transmissions of He^+, N^{2+}, B^+, C^+, N^+, P^{2+}, and O^+ ions as a function of RFQ electrode voltage

factor (VFAC), where the design inter-electrode voltage of 54.9 kV corresponds to 1.0 in VFAC. The beam transmissions are above 80 % for all the ion species. Fig. 3 shows the transmission of He^+ and B^+ ions as a function of un-normalized emittances of the injected ion beams. The expected un-normalized input emittance of an ion beam at the RFQ entrance is roughly 63 π mm-mrad in both horizontal and vertical directions. The calculated un-normalized output emittances of 90 % of transmitted particles of a He^+ ion beam is 9.2 and 12.3 π mm-mrad in horizontal and vertical directions, respectively. Assuming the same input emittances, we have found by calculation that the output emittances become smaller for heavier particles. For a B^+ ion beam they are smaller by roughly 10 % from the He^+ case. Fig. 3 shows that the beam transmission of 80 % is guaranteed up to the input emittance of 400 π mm-mrad for a B^+ ion beam. The ratio of the expected emittance to the calculated acceptance of the RFQ is more than 4. Fig. 4 shows the transmission of He^+ and B^+ ions as a function of the injection energies. The overall tendency is that up to ±5 % variation in injection energies is tolerable to achieve 80 % beam transmission. This gives no difficulty for present commercial high-voltage power supplies. Fig. 5 shows the beam transmission of He^+ and B^+ ions as a function of beam current. Up to a few mA of B^+ ions can be accelerated to the goal energy with 80 % beam transmission. For lighter ions and higher currents on the other hand, the space-charge repulsion force becomes predominant and it impairs the beam transmission. From those computer simulation runs, a proof has made that various ions can be accelerated with reasonable transmission and intensity in an RFQ and also that it has a large acceptance and relatively large tolerances in the variation of the injection energies.

4. Mechanical design of the RFQ

There are several unique features in the mechanical design of our 4-rod RFQ. The first is that the beam optics axis is not the center of the RFQ tank, but is eccentrically situated. This reduces the tank

diameter of the RFQ without any drastic change in the rf characteristics, lowering the costs of the RFQ cavity and vacuum system [26]. The second is concerned with how the vertical electrode supporting plates—what we call "posts"—are arranged so that both low resonant frequency and good longitudinal field distribution are achieved simultaneously. From our model studies, we have found that a 4-rod structure with equally-spaced posts has a very flat field distributions and it is well suited for a practical low frequency RFQ [20, 26]. This is different from a concept proposed by a group of Frankfurt university [19], in that a pair of posts are positioned close together in a unit module. The third is that the cross-section of the RFQ electrode is not circular rod [19,37,38] but rectangular and the machining of the "rod" has been made three dimensionally. Moreover all the parts in the RFQ electrode assembly is de mountable. We expect this "modified" rod electrode structure is more suitable for an industrial environment where a periodical maintenance is expected. The alignment of such "modified" rod electrodes can be done relatively easier because all the electrode surfaces except for the quadrupole tip can be machined precisely flat. The alignment jigs become simple and the associated work can be less laborious because those flat surfaces can be all used as reference. Also the handling and transportation of the electrodes require less care. The forth is related to cooling of the electrode assembly. This subject has a lot to do with the mechanical structure of the RFQ because all the parts inside the RFQ cavity are going to be heated with rf. The structure of the RFQ has to be simple and the number of parts should be small.

Fig. 6 is an exterior view of the RFQ cavity. The total length of the cavity is 2340 mm and the inner diameter is 600 mm. The material of the cavity is copper and the thickness of the cavity wall is 35 mm. The cavity consists of two identical tanks joined together at the middle. Each tank has five ports for a vacuum pump, a view window, a RF power drive, a RF monitor, and a loop-tuner. There are four view windows in the end-flange of the cavity. Each tank has four cooling pipes half-embedded and silver-brazed in the outer surface. A portion of the inner surface at the bottom of the cavity is machined flat so that the RFQ electrode assembly can be positioned

in place and it gets a good electrical contact with the inner wall of the cavity.

Fig. 7 is a view of RFQ electrode assembly as installed in the cavity. It consists of three major components : the RFQ electrodes, the electrode-supporting posts, and the base-plate. The material is all copper. A part of the accelerator section of the machined RFQ electrodes are shown in fig. 8. The whole assembly is put together outside the cavity using alignment jigs It is then installed and secured to the cavity. The number of the posts are six—this means a pair of RFQ electrodes is supported by three posts. The width and thickness of the posts are 240 mm and 45 mm, respectively. The beam optics axis is 330 mm above the upper surface of the base plate. The posts are equally spaced by 405 mm from each other.

There are three independent cooling-water channels allocated exclusively for the RFQ electrode assembly: two for the electrodes and one for the electrode-supporting posts and base plate. Approximately 20 liter/min of cooling water can flow through in each channel at pressure of 3.0 kgf/cm^2 This is adequate for 50 kW cw operation. The details on this subject can be found in ref.[39].

The vacuum system is comprised of two 900 l/min oil-rotary pumps and two 2000 l/sec turbo molecular pumps with a fully-automated control system. A typical vacuum level is 7.0×10^{-7} Torr when rf is off.

5. Injection system

A proper design of the Low Energy Beam Transport (LEBT) section to the RFQ is crucial for the performance of an RFQ linac. This premise should be emphasized when dealing with a high-current and low-β ion beam. There are basically two causes of beam degradation: one is to do with internal self-fields of the beam and the other to the second and higher order aberrations in the external force-fields produced by the ion optical systems. Since a brief summary of the ion injector to the RFQ has been described in ref. [40], details are given in this report.

5.1 Self-fields of the ion beam

Transport of a low-β ion beam presents particular difficulties because of its self-fields. In a particular case of positive ions, the space-charge force of the beam can be neutralized if proper cares are taken not to strip off stationary electrons which reside in the beam. In that case the beam blow up is suppressed and we can have a smaller beam through out the transport line. The costs and size of the optical components in such a beam line becomes considerably economical and sound. This can be easily understood by studying the envelope equation of laminar (zero emittance) beam introduced by Lawson, where the ratio of the maximum beam radius (r_m) to the initial beam radius (r_0) is expressed in terms of the generalized perveance (K) and the characteristic current (I_0) [41]:

$$\frac{r_m}{r_0} = 1 + 0.48K\left(\frac{z}{r_0}\right)^2, \qquad (13)$$

where z = drift distance [m],

$$K = \frac{I}{I_o}\frac{2}{\beta^3\gamma}\left(\frac{1}{\gamma^2} - f_e\right), \qquad (14)$$

and

$$I_0 = 3.1\times10^7\frac{A}{Z}\ [A]. \qquad (15)$$

The quantities in eqs. (14) and (15) are defined as follows:

I = beam current [A],

β = velocity of particle/c,

$\gamma = (1 \quad \beta^2)^{-1/2}$,

f_e = ratio of electron charge to positive ion charge per unit volume,

A = ion mass in AMU, and
Z = ion charge.

Equation (13) indicates that in non-relativistic and without space-charge neutralization (when $f_e=0$), the beam expansion is proportional to β^{-3} This becomes a dominant term at low energy as β approaches zero. It is also interesting to note that the beam expansion is proportional to r_0^{-2}: larger the initial beam size, easier the beam transport. Fig. 9 clarifies those points by showing the plots of the drift distance of doubling beam size as a function of beam current. In a practical case, for instance, when the beam current is an order of mA and the beam radius of 10 mm, one can see that the beam doubles in its size as it propagates in field-free region by one meter, assuming the initial angular divergence is zero. On the other hand in fully-neutralized case when $1/\gamma^2=f_e$, K vanishes so that the beam diameter remains constant if the angular divergence of the initial beam is zero. We assume that this charge neutralization is preserved in our LEBT section so that beam current can be practically set to zero in the following ion optics calculations

5.2. LEBT optics

Beam optics calculation is done first using TRACE 3-D [42]. An ion beam of 30 keV single-charged boron, which is extracted from the rectangular slit of the Freeman source, is followed through the optical elements. At the entrance of the RFQ, the ion beam is focused into a near round shape to match the RFQ. An Einzel lens has to be added just upstream of the RFQ entrance to get the mismatch factor defined in TRACE 3-D less than 0.1.

The optics calculations are redone and checked to the second order using TRANSPORT [43]. The results of the second order calculations on TRANSPORT shows the degradation of the beam. The comparisons of the first and the second order calculations can be made clear by observing fig. 10, in which the differences in beam envelope size normalized to the first order calculations are plotted for both with and without the second order corrections. The beam

envelope size without the second order corrections is larger approximately by 8 % at the RFQ entrance and there are considerable displacements of the beam centroids in the final beam trace-space. Those results cannot be neglected if we were to achieve an ideal beam transmission in the LEBT and RFQ. The corrections are made to the analyzing magnet by including sextupole components [44]. The results are very satisfactory as can be seen in fig. 10 and in table 3; the increase in the beam sizes is below 0.1 %, the degradation in the beam divergence become less than 0.4 %, and the shifts of the beam trace-space centroids settle at permissible level. Fig. 11 shows the beam envelope plots of a 30 keV B^+ ion beam from the souce to the entrance of the RFQ.

5.2.1. Construction

The injector comprises a Freeman ion source, a 90 degree analyzing magnet, quadrupole magnets, and a HV cabinet in which a programmable controller sub-system, gas flow system, and ion source power supplies are all housed. The vacuum system is comprised of a 550 l/sec turbo molecular pump and a 350 l/min oil rotary pump. All those beam optical, electrical, and vacuum components are arranged and installed in the X-ray shielded cabinet. Fig. 12 is an interior view of the injector taken from the ion source side. Small size and easy maintainability is sought in the design of the injector. The descriptions of the components are as follows:

Ion source

A Freeman type "medium-current" ion source frequently used in industry is adopted [45]. This ion source delivers a mA class single-charged boron ion beam at 30 keV extraction voltage.

Analyzing magnet

Fig. 13 is the drawing of the 90 degree analyzing magnet. The magnet has rotatable entrance and exit pole pieces for the fine correction of the beam trajectories. The magnetic boundary is approximately that of Rogowski type [46,47]. The mass resolution $M/\Delta M$ at F.W.H.M. is more than 100. The maximum attainable magnetic rigidity $B\rho$ of the magnet is 8.01 kG·m. The sextupole corrections are made to the poles and magnet boundaries to improve the beam quality. Fig. 14 shows the calculated magnetic field lines of the analyzer magnet. Only one quarter of the magnet is shown in the figure.

Quadrupole magnets

Fig. 15 is a drawing of the quadrupole magnet lenses. There are four quadrupoles, which are all identical in construction. The result of field calculation is shown in fig. 16. The multipole components—12 and 20-pole—of magnetic field are minimized to less than 0.2 % in the design. The magnet coils are vacuum impregnated with epoxy-resin that has high thermal-conductivity and they are indirectly cooled by water. The temperature stability of the coil is greatly improved in this design—the temperature rise is only 5 °C with 1.8 liter/min cooling water in the 220 turn coil at the current of 20 A. The field gradient of 17 T/m is attainable at this current and it is more than adequate in our requirement.

6. rf power amplifier system

Fig. 17 is a block diagram of and fig. 18 is a picture of the rf power amplifier (P.A.) system. Both the 50 kW P.A. and the 5 kW P.A. have a local as well as a remote controller. The two 5 kW P.A.s are identical : one is used as a driver amplifier for the 50 kW P.A. and the other is going to be used as a final-stage P.A. for the additional accel./decel. cavity. A 5 kW P.A. system consists of a 500 W solid-state driver amplifier and a Siemens RS3021 CJ triode P.A. in the final stage. The 50 kW P.A. is also a tube-amplifier equipped with a Siemens RS2058 CJ tetrode. RS3021 CJ and RS2058 CJ have the

maximum anode dissipation of 20 kW and 90 kW, respectively. The reason we have chosen such large tubes is that small-size circulator is not easily available in this frequency regime. It can be thought as one practical way of protective measures for the expensive tubes.

The total power required for the full power operation of the 50 kW and 5 kW system is approximately 140 kVA. The rf P.A. system also requires 100 liters/min. of de ionized-water for cooling. This P.A. system is expandable to meet for multi-accel./decel. cavities by adding the phase shifting units to the existing P.A. system. An upgrade in the linac's maximum energy or its energy range can be accomplished without major change in the P.A. system configuration.

The 50 kW final stage P.A. is classified as cathode-driven class AB rf amplifier. The driver amplifier's output is fed to the cathode via WX-39D. The output is transmitted to the RFQ cavity in WX-77D coaxial tube. The power efficiency that is defined as RF power output divided by power fed to the RS2058 CJ's anode is approximately 70 % at 50 kW output. The output ripple is less than ±2% at the maximum output. The higher harmonics are kept below -30 dB at the same output level. The cabinets of P.A.s are properly RF shielded to satisfy the applicable regulatory standard. This is checked with a commercial RF survey meter and by more sensitive electric field strength measurement with an antenna and a spectrum analyzer. At 50 kW output loaded into a dummy, rf leak is undetectable anywhere in the vicinity even in the lowest range (full scale being 2.65×10^{-2} mW/cm^2) of the survey meter. Detailed descriptions on this rf P.A. system is found in ref. [48].

7. Control system

The control system of the RFQ comprises basically three independent sub-control systems which are specified in its function: the rf P.A., the vacuum and ion source, and the data acquisition and beam transport. Since the system configuration of the rf P.A. is already described in the previous chapter, only a block diagram of the other two sub-control systems is shown in fig. 19. The vacuum and ion source controller is built on commercially available

programmable controllers linked in optical fiber network. There are two man-machine interface panels from which an operator can interact with the system. This is a backbone of our RFQ linac control system enabling an operator to execute an automated sequences of the vacuum system and to control the ion source system. A secure operation is guaranteed with interlocks. The control of data acquisition apparatuses and beam optical components in the transport line is based on a personal computer (PC) and a data acquisition crate linked in GP-IB. This PC based data aquisition system is versatile and expandable to meet any experimental situation in the future. All the control and monitoring can be done via GUI (Graphic User Interface) on the computer monitor screen. Fig. 20 is one example of such GUI control panels realized on the PC.

8. Measurments of rf characteristics — cold test

8.1. rf characteristics of 4-rod RFQ with copper un-modulated electrodes and aluminum posts

Cooling and vacuum engineering won't be practical if the power efficiency of the cavity is too low because our 4-rod RFQ is used in cw operation. Therefore the Q-value and the shunt impedance R_O of the cavity are the most important parameters in our RFQ design. The longitudinal electric-field distributions and the balance of the quadrupole strength are also important properties of the RFQ. Thus we have measured rf characteristics of our 4-rod RFQ with un-modulated electrodes before machining the modulated electrodes.

8.1.1. Measurements of Qo and Ro/Qo

One common way to determine RFQ's power requirement is to measure both R_O/Q_O and unloaded Q-value (Q_O) and then to estimate the shunt impedance (R_O) of the accelerator cavity. We have attempted to determine R_O/Q_O by two different ways: bead-pull and so-called "capacity variation" (c.v.) method [49-51]. Q_O, perturbed resonant frequency (f), and unperturbed resonant frequency (f_O) are

measured with a network analyzer. The measured value of Q_0 by "transmission method" is approximately 5000. This value of Q_0 is used throughout later calculations.

The result of bead-pull in transverse direction is shown in fig. 21. The bead is a metallic sphere 3 mm in diameter. R_0/Q_0 is calculated as follows [50] :

$$\frac{R_0}{Q_0} = -\frac{2S^2}{k\omega\varepsilon f}\frac{\Delta f}{\Delta\tau}, \qquad (16)$$

where S = 7 mm is the minimum distance between electrodes,
k = 3,
w = 2π f, where f is resonant frequency,
ε = permittivity of free space,
$\Delta f = f \quad f_0$,
$\Delta\tau$ = volume of perturber.

R_0/Q_0 is calculated to be 18.9 Ω. R_0 is then estimated to be 94.5 kΩ per cavity. The required power to excite the RFQ cavity at the design inter-electrode of 54.9 kV is estimated to be 15.9 kW

Capacity variation method is schematically depicted in fig. 22. The idea is to perturb the inter-electrode capacitance of one quadrant of the RFQ by putting a small capacitor. The net inter-electrode capacitance then increases and the resonant frequency shifts lower. R_0/Q_0 is determined as follows [51]:

$$\frac{R_0}{Q_0} = -\frac{2}{\omega_0^2}\frac{d\omega}{dc}, \qquad (17)$$

where $w_0 = 2\pi f_0$,
w = 2π f, where f is perturbed resonant frequency,
c = perturbing capacitance.

The average value of R_0/Q_0 among the four quadrants is used to estimate rf power requirement and the variations of R_0/Q_0 can be interpreted as representation of the quadrupole field balance.

Fig. 23 shows plots of resonant frequencies vs. capacitance in all four quadrants of the RFQ. Perturbing capacitance is about 10 pF and it is small compared with the effective inter-electrode capacitance which is approximately 75 pF/quadrant from calculations using POISSON. The slopes of the curves dω/dc are found by liner-fits. The average value of dw/dc of quadrant 1 and 3 is $2\pi(-0.0510)$ MHz/pF. R_O/Q_O is then calculated to be 14.4 Ω. This value is roughly comparable to the result obtained from the previously described transverse bead-pull measurements. We observed a slight increase of the unperturbed resonant frequency in the measurements by the capacity variation method. This was due to the installation of cooling pipes in the RFQ cavity after the bead-pull measurements. Quadrupole electric-field strength is roughly 6 % higher in quadrant 2 and 5 % lower in quadrant 4, compared with the average electric-field strength of quadrant 1 and 3. This difference is compared with the result of measurements of longitudinal field distribution in the following sub-section.

8.1.2. Longitudinal electric-field distributions

Because the RFQ cavity is rather long, a particular attention has to be given to the measurement setup of longitudinal bead-pull: weight of perturber, perturbation due to the thread, and the alignment of and tension in the thread. The bead is a plastic cylinder 8 mm in diameter and 11 mm in length. The diameter of a fishing thread is 0.22 mm. Unperturbed resonant frequency is measured for each setup of measurement when the perturber is pulled out of the cavity but the thread remaining in the cavity. Fig. 24 shows the results of bead pull along the longitudinal axis in all four quadrants of the RFQ. The observation of fig. 24 indicates that the longitudinal electric-field strength is flat within ±4 % in each quadrant and that the quadrupole electric-field strength is higher by roughly 6 % in quadrant 2 and lower by roughly 6 % in quadrant 4, compared with the average value of quadrant 1 and 3. Those agree with the results obtained by the capacity variation method.

8.2. rf characteristics of 4-rod RFQ with copper modulated electrodes and copper posts

We have checked the values of R_o/Q_o and Q_o after installing the modulated electrodes in the RFQ assembly. Only the capacitance variation method was used to measure R_o/Q_o. Fig. 25 shows the results and they are identical with the results obtained earlier with the un-modulated electrodes. An average value of R_o/Q_o in quadrant 1 and 3 was 14.4 Ω. Then the value of R_o is estimated to be 47.6 kΩ per cavity from the measured value of Q_o, 3300. The degradation of Q_o may be due to the increase of electrical losses in the contact between the posts and the rod RFQ electrodes; the electrical contact is poorer in copper-copper boundary than aluminum-copper boundary.

8.4. Summary.

The rf characteristics of the 4-rod RFQ are summarized in table 4 and 5. It is demonstrated in the experiments that our 4-rod RFQ has a very flat electric-field distribution along the longitudinal direction and a slight asymmetry in its quadrupole field. These are general properties of this type of RFQ, however, the effect of the latter doesn't cause much problem in a practical situation. This zeroth order error is a reflection of the asymmetry of the RFQ electrode supporting structure, and it results in an offset of the beam optics axis by corresponding proportion.

9. High power rf tests

The purposes of high power rf tests were to check the rf and temperature stability of the 4-rod RFQ and also to survey both the rf and X-rays leaks from the RFQ cavity.

Fig. 26 shows the temperature rises of cooling water in the RFQ assembly up to 40 kW of cw rf power. The temperature of cooling medium was measured with thermocouples placed on the metal joints in the water channel of the RFQ electrode assembly. Since there was about 30 seconds of a transient period after the rf power was set

to a new value, all the data were taken after the readings of the temperature were frozen. An estimation using the data in fig. 26 suggests that almost 90 % of the rf power put into the RFQ cavity was spent only in the RFQ electrode assembly. Fig. 27 is a plot of the resonant frequency of the RFQ as a function of cw rf power. The same precaution was made in this measurement too as to the timing of reading. We encountered no sparking in the RFQ cavity during this experiment except in the very beginning of the power feeding when the cavity had been vented to the atmosphere. The vacuum pressure was below 1.8×10^{-6} Torr at any rf power level while the base pressure without rf was 1.0×10^{-6} Torr.

The rf leak was inspected with a commercial rf survey meter; the same one used in the test for the rf P.A. system. The electromagnetic radiation was undetectable even in the lowest range (full scale being 2.65×10^{-2} mW/cm^2) of the survey meter at 40 kW rf power level. The X-rays leak was examined with a survey meter at several points on the outer surface of the RFQ cavity. Under the same condition of rf power, the X-rays leak was less than 0.14 μS/h. This is well below the maximum exposure rate of 0.6 μS/h, below which the accelerator is not categorized as a radiation facility in a sense of the Japanese law of radiation control.

10. Beam acceleration tests

10.1 Experiment setup and beam diagnostic devices

Setup

Fig. 28 is a schematic layout of and fig. 29 is a picture of the RFQ linac system as installed in the Accelerator Lab. of ICR, Kyoto University. The experiment was planed to draw as much information as possible of both the input and output beam of the RFQ. The input and output beam current were measured with Faraday cups. The emittance of the beam in the trace-space of two orthogonal coordinates in the transverse plane of the ion optical axis were studied using the emittance monitors for the input as well as the output beam. The energy of the input beam could be known

accurately (better than ±0.5 %) by measuring a terminal voltage of the ion extraction high voltage power supply using an appropriate resistor divider. The output beam energy of the RFQ was estimated from a momentum spectrum of the beam, which was taken with the 15° degree bending magnet. Finally the most definite approach to identify the species and energy of an ion beam was to actually implant the ions to a silicon wafer and to take the range profile of the implanted ions by SIMS (secondary ion mass spectroscopy) analysis.

Faraday cup

There are five Faraday cups in total to measure the intensity of the ion beam. F1 is located just downstream of the beam defining slit in the 90° degree magnetic analyzer system. This retractable Faraday cup F1 practically works as a beam stopper as well as a measuring electrode to take a momentum spectrum of the beam from the ion source. F2 and F3 are retractable, too and true Faraday cups of the aperture to length ratio of three and with a secondary-electrons suppresser electrode. F2 and F3 are used to measure the intensity of the beam at the upstream and downstream of the RFQ, respectively. F4 and F5 are both true de-mountable Faraday cup systems installed at the end of a vacuum chamber. The systems are similar to those of F2 and F3.

Emittance monitor

The emittance monitors EM1 and EM2 are exactly identical. They are of "a slit and multi-wires" type. A schematic of the probe construction is shown in fig. 30 and the specification of the emittance monitor is summarized in table 6. The advantages of adopting this type of an emittance probe is its speed and easiness in the assembly and alignment work. One complete measurement in the two orthogonal directions takes only a minute in a typical run. On the other hand the disadvantages are that the angular resolution is limited primarily by the number of wires and their spacing. In both

EM1 and EM2 there are only 10 wires being used. The wires are separated by 3 mm. The construction is simple and the total costs is relatively low in such configuration however, the angular separation of the detector wires is such that only a rough measurement is possible in the present design. This was preferred anyway for the preliminary measurement of the beam emittances because the output beam from the RFQ was expected to have a large divergence of 50 mrad in case of a He^+ beam by PARMTEQ simulation. The performance of the emittance monitor will be upgraded to get better angular resolution in the future development.

10.2 Experimental results and analysis

Intensity

Fig. 31 is a plot of He^+ and N^{2+} ion beam transmission of the RFQ as a function of rf power. F2 and F3 Faradays cups were used for the measurements of the beam intensities of the input and output beam currents. Note that the value of ion beam current obtained at F3 represents a total un-analyzed beam current and that the Einzel lens was put off in all the N^{2+} beam runs. The values listed in table 7 typifies the results of this part of the beam experiment. The beam transmissions of He^+ approaches 90 % and those of N^{2+} and C^+ ion beam are approximately 80 %. These are in good agreement compared with the results of PARMTEQ simulation runs previously shown in fig. 2. The typical beam currents obtained at the RFQ output were 32, 13, and 220 pμA for He^+, N^{2+}, and C^+ ions, respectively. Lower transmission of N^{2+} and C^+ ion beams may be due to the mismatch in the orientation of the trace-space ellipses at the RFQ entrance.

Emittance

Fig. 32 shows the typical results of the beam emittance measurements for a He^+ ion beam. The measurements were done at the probe position of 233 mm upstream of and 388 mm downstream

of the RFQ electrode edges. The total beam currents at F2 and F3 were 27 μA and 21 μA, respectively. The rf power put into the RFQ was 20 kW In those figures, the trace-space ellipses obtained by the calculations using PARMTEQ and TRACE 3-D are superposed on the raster images of the measured emittance data. In PARMTEQ simulations, the beam parameters were extracted from the results of 90 % of the transmitted particles and in TRACE 3-D the last two cells of the RFQ were simulated as "normal cell" with no acceleration. No space charge was included in both PARMTEQ and TRACE 3-D calculations. Although the resolution for the angle is very poor, one can get a qualitative understanding in comparison with the calculations.

Momentum spectrum

The expected mass resolution M/ΔM of the 15 degree bending magnet is about 50. The current of a beam which is collimated through the slits located both at the entrance and the exit of the analyzing magnet system is measured by F5. Fig 33 shows the momentum spectra of He^+, N^{2+}, and C^+ ion beams accelerated by the RFQ. The energy of the accelerated beam were calibrated by extrapolating from the spectrum of a mono-energetic beam of the ion source coming through the RFQ—rf power is off so that there is no acceleration in the RFQ. The estimated output energies of He^+ and C^+ beams were 346 KeV ± 2 % and 1071 KeV ± 2%, respectively. These values differs by + 2.2 % and + 5.4 % from the output synchronous energies of He^+ and C^+ calculated by PARMTEQ , respectively.

Partially accelerated components

The energy spectra of a C^+ beam analyzed with the 15 degree bending magnet system are shown in fig. 34. Each spectrum was taken by scanning the magnet current from zero to an appropriate value at different rf power and a set of all the spectra were put in one graph to illustrate how the structure of the beam energies

changed with the rf power put into the RFQ cavity. Partially accelerated components of the C^+ beam became apparent as the rf power was brought down below 40 kW. A similar phenomenon was unexpectedly discovered first by on the accelerator test stand at Los Alamos National Laboratory [52] and its practical use was suggested by Shimadzu Corporation [53]. Fig. 35 shows the calculated energy spectra of a C^+ beam in varied rf power. The inter-electrode voltage is converted to the rf power assuming that VFAC=1.0 corresponds to 31.7 kW of the rf power. Though the absolute values of the rf power don't coincide between the experiments and calculations, the calculated shapes of the energy spectra are discovered to be quite similar to the experiment.

SIMS analysis of implanted ions

SIMS analysis is nowadays one of the most popular evaluation techniques among the semiconductor device manufactures due to the results of a rapid spread of commercial SIMS tools. It is often the case that this analysis is used to examine quantitatively the contamination that may brought into the silicon wafers in the processes of integrated circuit manufacturing. There are also an scientific studies done on the range profile of MeV implantation by SIMS analysis [54,55]. Fig. 36 shows the range profile of N^{2+} beam implanted in a silicon wafer at dose of approximately 1×10^{16} atoms/cm^2. The rf power to the RFQ is 20 kW and the expected energy of the N^{2+} beam is 1.17 MeV The peak of the profile corresponds to the range of 1.6 μm which deduces the energy of the N^{2+} beam to be approximately 1.1 MeV from the data in ref.[2,54,55]. This is in a fairy good agreement.

11. Conclusion and discussion

A cw "modified" 4-rod RFQ linac has been designed, constructed, and successfully tested. The criterion described in section 2 of "general considerations" are all fulfilled to satisfactory

levels. The RFQ's size and its performances are suitable to the use of this type of rf linac for irradiation of light and heavy ions with energies up to a few MeV. Improvement of the Q-value of the RFQ will reduce rf power consumption and the utility requirement. A summation of the initial and operating costs will then become an important item for industrial uses. In the beam experiments we have observed that to increase the inter-electrode voltage of the RFQ, more rf power was needed than expected from the low power measurements. The power requirement in accelerating C^+ doesn't scale with the those cases of He^+ and N^{2+} It suggests that the temperature increase in the RFQ assembly degrades the Q-value at the high power operation. This should be another point that an improvement is necessary. We all hope that this work will somehow awaken potential users to consider a possibility of using a MeV ion implanter of this type and we could help in the near future contribute to their progress and successes in the various fields of research and technology.

Acknowledgments

The author would like to appreciate all the staff members of The Accelerator Laboratory of The Institute of Chemical Research, Kyoto University, particularly Prof. Emeritus Hidekuni Takekoshi, Profs. Makoto Inoue and Akira Noda, Drs. Yoshihisa Iwashita and Hiromi Okamoto. They have provided the author with invaluable help and instruction in all phases of this work. Experiences and confidence that have developed during the author's stay at their laboratory will become an irreplaceable treasure for the rest of his carrier. Gratitude goes to many people at Nissin, especially senior managing director Mr. Fumio Fujiki, manager of Ion Equipment div. Mr. Masatoshi Harada, deputy managers of Ion Equipment div. Mr. Tadashi Kawai and Mr. Sadao Tsuji, and senior research engineer Mr. Masao Naito. This work was accomplished with their support and encouragement in an extended period of his research and development activity. Special thanks go to section chief of Seiki dep.

Mr. Tetsuo Shimizu who directed the manufacturing of the RFQ electrodes and the other crucial components of the linac. Thanks are also extended to the author's colleagues, Mr. Toshihiko Katagiri, Mr. Masatoshi Tamada, and Mr. Takao Matsumoto with whom the author always have enjoyed working. Their superb and efficient work accelerated the progress of this project and led to a successful result. There are so many who have involved in this work directly and indirectly besides above mentioned people. The author would like to thank them all and apologize that he cannot accredit them here.

References

[1] D. Pramanik and M. Current, "MeV Implantation for Silicon Device Fabrication", Solid State Technology, (May 1984) 211.

[2] J.F. Ziegler, "High Energy Ion Implantation", Nucl. Inst. and Meth. B6 (1985) 270.

[3] D. Pramanik and A.N. Saxena, "MeV Implantation for VLSI", Nucl. Inst. and Meth. B10/11 (1985) 493.

[4] K.W Terrill, P.F Byrne, C. Hu and N.W. Cheung, submitted to Elec. Dev. Lett.

[5] C. McKenna, C. Russo, B. Pedersen, D. Downey and R. Liebert, "Applications for MeV Ion Implantation", Semiconductor International (April 1986).

[6] H.F Glavish, D. Bernhard, P Boisseau, B. Libby, G. Simcox and A.S. Denholm, "Production High Energy Ion Implanters Using Radio Frequency Acceleration", Nucl. Inst. and Meth. B21 (1987) 264.

[7] N. Turner, K.H. Purser and M. Sieradzki, "Design Considerations of a VLSI Compatible Production MeV Ion Implantation System", Nucl. Inst. and Meth. B21 (1987) 285.

[8] I. Kapchinskii and V Tepliakov, Pub. Tekh, Eksp., No. 2, 19 (1970).

[9] R.W. Hamm et al., Proc. Int. Conf. on Low Energy Ion Beams 2, Univ. of Bath (1980).

[10] K. Bethge, "Accelerators in Industrial Applications", 1988 European Particle Accelerator Conference Proceedings, World Scientific Publishing Co. pte. ltd. (1988) 158.

[11] A. Schempp, "The Application of RFQs", 1992 Linear Accelerator Conference Proceedings, AECL-10728 (1993) 545.

[12] W.R. Fahrner, J.R. Laschinski and D. Braunig, "Application of High Energy Implantation in Semiconductors", Nucl. Inst. and Meth. A268 (1988) 579

[13] A. Chayahara, M. Kiuchi, Y. Horino, K. Fujii and M. Satou, "Surface Modification by MeV Ion Implantation", Jpn. J. appl. Phys. Vol. 60 No. 7 (1991) 674.

[14] K. Tsukamoto, S. Komori, T. Kuroi and Y. Akasaka, "High Energy Ion Implantation in Semiconductor Processing", Jpn. J. appl. Phys. Vol. 60, No. 11 (1991) 1087.

[15] Review articles on high energy ion implantation in Nikkei Microdevices (Dec. 1991) 94.

[16] K. Tsukamoto, S. Komori, T. Kuroi and Y. Akasaka, "High-energy Ion Implantation for ULSI", Nucl. Inst. and Meth. B59/60 (1991) 584.
[17] K. Tsukamoto, S. Komori and T. Kuroi, "High-energy Ion Implantation", Ion Engineering Vol. 1, No. 1 (May 1992).
[18] A. Schempp et al., 1984 Linear Accelerator Conference Proceedings, GSI-84-11 (1984)100.
[19] A. Schempp, H. Deitinghoff, M. Ferch, P Junior and H. Klein, "Four-Rod-λ/2-RFQ for Light Ion Acceleration", Nucl. Inst. and Meth. B10/11 (1985) 831.
[20] T. Ogawa and Y Iwashita, "Model Study of a 4-rod Structure of RFQ Linac", Bull. Inst. Chem. Res. Kyoto Univ. Vol. 65, No. 1 (1987) 51.
[21] H. Fujisawa, Y. Iwashita and H. Takekoshi, "4-rod RFQ Proton Acceleration Tests", Proceedings of The 13th Linear Accelerator Meeting in Japan (1988)71.
[22] H. Fujisawa, Y. Iwashita and H. Takekoshi, "4-rod RFQ Proton Acceleration Tests", Bull. Inst. Chem. Res. Kyoto Univ. Vol. 67, No. 1 (1989)7
[23] H. Fujisawa, Y. Iwashita and H. Takekoshi, "Proton Acceleration Tests on the 4-rod RFQ & QWR", Proceedings of The 14th Linear Accelerator Meeting in Japan (1989)298.
[24] H. Fujisawa and M. Naito, "Research on rf Accelerators for MeV Ion Implantation System", Nissin Electric Co., Ltd. Technical Journal, Vol.35, No.2 (March 1990).
[25] H. Fujisawa, Y. Iwashita and H. Takekoshi, "Design Study of a Heavy Ion RFQ Linac", Bull. Inst. Chem. Res. Kyoto Univ. Vol. 68, No. 2 (1990)121.
[26] H. Fujisawa, Y Iwashita, M. Inoue and H. Takekoshi, "Design Study of a Heavy Ion RF Linac for MeV Implanter", 1990 Linear Accelerator Conference Proceedings, LA-12004-C (1991)241.
[27] S. Wolfram, "*Mathematica*®, a System for Doing Mathmatics by Computer", Second Edition, Adison-Wesley Publishing Company, Inc.(1991).
[28] S. Yamada, "Buncher Section Optimization of Heavy Ion RFQ Linac", 1981 Linear Accelerator Conference Proceedings (1981)316.
[29] T. Nakanishi et al., "Construction and Operation of a Test RFQ Linac for Heavey Ions", Particle Accelerators, Vol.20 (1987)183.
[30] T. Nakanishi, "Study of an RFQ Linac of a Four-Vane Type for Medium Heavy Ions", Ph.D. dissertation, Nihon University.

[31] K.R. Crandall, R.H. Stokes and T.P. Wangler, "RF Quadrupole Beam Dynamics Design Studies", BNL-51134 (1979) 205.
[32] T.P. Wangler, "Space-Charge Limits in Linear Accelarators", LA-8388, Los Alamos National Laboratory(1980).
[33] R.A. Jameson, LINACS, a *Mathematica*® version of CURLI code, Los Alamos National Laboratory(1990).
[34] W.D. Kilpatrick, "Criterion for Vacuum Sparking Designed to Include Both rf and dc", Rev. of Sci. Instr.. Vol. 28, No. 10(1957)824.
[35] K.R. Crandall, "Effects of Vane-Tip Geometry on the Electric Fields in Radio-Frequency Quadrupole Linacs", Los Alamos National Laboratory report, LA-9695-MS (1983).
[36] K.R. Crandall, R.S. Mills and T.P Wangler, "Radio-Frequency Quadrupole Vane-Tip Geometries", IEEE Transactions on Nuclear Sience, Vol. NS-30, No. 4 (1983) 3554.
[37] A. Schempp, "RFQ Ion Accelerators", Nucl. Inst. and Meth. B45 (1990) 302.
[38] A. Schempp and H. Deitinghoff, "Properties of RFQ Accelerators for Ion Implantation", Nucl. Inst. and Meth. B68 (1992) 36.
[39] H. Fujisawa, M. Tamada, T. Katagiri, Y. Iwashita and H. Takekoshi, "Mechanical Design of 33.3 MHz 4-rod Heavy Ion RFQ Cavity", Bull. Inst. Chem. Res. Kyoto Univ. Vol. 70, No. 1 (1992) 28.
[40] H. Fujisawa, M. Tamada and T. Matsumoto, "An Injector to the 33 MHz 4-rod RFQ", Bull. Inst. Chem. Res. Kyoto Univ. Vol. 71, No. 1 (1993)1
[41] J.D. Lawson,"The Physics of Charged-Particle Beams", Ch.3.2.8, Oxford Science Publications, Second Edition (1988).
[42] K.R. Crandall, revised by D.P Rusthoi, "TRACE 3-D Documentation", Second Edition, LA-UR-90-4146 (1984).
[43] K.L. Brown, D.C. Carey, Ch. Iselin and F. Rothacker, "TRANSPORT, a Computer Program for Designing Charged Particle Beam Transport Systems", CERN 80-04 (1980).
[44] H.F. Glavish, "Magnet Optics for Beam Transport" , Nucl. Inst. and Meth., 189 (1981) 43.
[45] Ion Equipment Division, Nissin Electric. Co. Ltd., 575 Kuze Tonoshiro-cho, Minami-ku, Kyoto 601 Japan.
[46] Harald A. Enge, "Converting an Ion-Optical Layout Into the Design of a Practical Magnet System", Proceedings of the International Symposium on Magnet Technology (1965).

[47] C.M. Braams, "Edge Effect in Charged-Particle Analyzing Magnets", Nucl. Inst. Meth., 26 , (1964) 83.
[48] Hiroshi Fujisawa, "The RF Power Amplifier System for a Heavy Ion RFQ Linac", Bull. Inst. Chem. Res. Kyoto Univ. Vol. 69, No. 1 (1991)11.
[49] R.H. Stokes, et al., "A Spiral-Resonator Radio-Frequency Quadrupole Accelerator Structure", IEEE Trans. Nucl. Sci. Vol. NS-30, No. 4 (1983) 3530.
[50] E.L. Ginzton, "Microwave Measurements", McGraw-Hill, New York, Sec. 10.4 (1975).
[51] Ibid., Sec. 10.2.
[52] G.P. Boicourt, O.R. Sander and T.P. Wangler, "Comparison of Simulation with Experiment in an RFQ", IEEE Transactions on Nuclear Science, Vol. NS-32, No. 5 (1985) 2562.
[53] A. Hirakimoto, H. Nakanishi and M. Asari, "The MeV Ion Implantation system RFQ-1000 and its applications", Nucl. Inst. and Meth., B55 (1991) 493.
[54] H. Wong, E. Deng, N.W. Cheung, P.K. Chu, E.M. Strathman and M.D. Strathman, "Profile Studies of MeV Ions Implanted into Si", Nucl. Inst. and Meth., B21 (1987) 447.
[55] D.C. Ingram, J.A. Baker, D.A. Walsh and E. Strathman, "Range Distributions of MeV Implants in Silicon 2", Nucl. Inst. and Meth., B21 (1987) 460.

Figure Captions

Fig. 1: RFQ electrode parameters obtained in OPTIMIZER runs. Synchronous energy (W_S), minimum aperture radius (a), modulation factor (m), focusing strength (B), and synchronous phase (ϕ_S) are plotted as a function of cell number.

Fig. 2: Plots of calculated beam transmission as a function of VFAC (RFQ inter-electrode voltage factor) for several ions of interests. Injection energy is 2.7 keV/u. for all cases. 100 particles are followed through at zero current with ELIMIT set to 5 % value of the final synchronous energy. Input beam parameters are fixed for all calculations : α = 0.45, β = 0.1 mm/mrad, and un-normalized emittance = 289 π mm-mrad.

Fig. 3: Plots of calculated beam transmission as a function of un-normalized emittance for B^+ and He^+ Injection energy is 2.7 keV/u for all cases. 100 particles are followed through at zero current with ELIMIT set to 5 % value of the final synchronous energy. Input beam parameters are fixed for all calculations : α = 0.45 and β = 0.1 mm/mrad.

Fig. 4: Plots of calculated beam transmission as a function of the injection energies of B^+ and He^+ 100 particles are followed through at zero current with ELIMIT set to 5% value of the final synchronous energy. Input beam parameters are fixed: α = 0.45, β = 0.1 mm/mrad, and un-normalized emittance = 289 π mm-mrad.

Fig. 5: Plots of calculated beam transmission as a function of the injection current of B^+ and He^+ Injection energy is 2.7 keV/u for all cases. 100 particles are followed through with ELIMIT set to 5% value of the final synchronous energy. Fixed parameters are input beam parameters, α = 0.45 and β = 0.1 mm/mrad ; and VFAC, 1.1 and 0.8 for B^+ and He^+, respectively.

Fig. 6: Exterior view of the RFQ cavity.

Fig. 7: View of RFQ electrode assembly as installed in the RFQ cavity.

Fig. 8: Part of the accelerator section of the machined RFQ electrodes.

Fig. 9: Plot of the drift distance of doubling beam size as a function of beam current for six different values of the initial beam sizes. The results are obtained by finding the solutions of the beam envelope equation defined by Lawson [44]. The beam is assumed as laminar (beam with zero emittance) and non-relativistic ion beam.

Fig. 10: Differences in beam envelope size normalized to the first order calculations are plotted along the beam transport line for both with and without the second order corrections. 45° degree coordinate transformation is performed at the end of the LEBT section. This is why it is two valued at the corresponding point. H and V correspond to horizontal and vertical planes, respectively.
Fig. 11: Beam envelope plots of a 30 keV B^+ ion beam in the LEBT. Q and E stands for quadrupole and Einzel lens, respectively.
Fig. 12: Interior view of the ion beam injector taken from the ion source side.
Fig. 13: Drawings of the 90 degree analyzing magnet.
Fig. 14: Calculated field distribution of the 90 degree analyzing magnet.
Fig. 15: Drawings of the magnetic quadrupole lenses.
Fig. 16: Calculated field distribution of a quadrupole magnet.
Fig. 17: Block diagram of the rf power amplifier system.
Fig. 18: Picture of the rf power amplifier system.
Fig. 19: Block diagram of the control system for the RFQ linac. Only the sub-control systems of the vacuum-ion source and the data acquisition-beam transport components are shown.
Fig. 20: An example of GUI control panels realized on the PC.
Fig. 21: Results of bead-pull in the transverse direction of the RFQ. The RFQ electrodes are un-modulated and the posts are made of aluminum.
Fig. 22: Schematic representation of capacity variation method.
Fig. 23: Determining of Ro/Qo and the quadrupole field balance by "capacity variation" method. A small ceramic capacitor is coupled to the adjacent RFQ electrodes in order to perturb the inter-electrode capacitance of RFQ. The variations in resonant frequency are plotted against the value of capacitance in all four quadrants of the RFQ. Electrodes are un-modulated.
Fig. 24: Results of bead-pull along the longitudinal axis in all four quadrants of the RFQ. The bead is positioned interior of RFQ field. The bead is made from plastic cylinder and the dimension is 8 mm in diameter and 11 mm in length. RFQ electrodes are un-modulated and the posts are made of aluminum.

Fig. 25: Plot of resonant frequencies vs. capacitance in all four quadrants of the RFQ with modulated electrodes in capacitance variation measurements.
Fig. 26: Plot of temperature rises of cooling water in the RFQ assembly as a function of cw rf power.
Fig. 27: Plot of the resonant frequencies of the RFQ as a function of cw rf power.
Fig. 28: Schematic layout of the RFQ linac system as installed in the Accelerator Lab. of ICR, Kyoto University.
Fig. 29: Picture of the RFQ linac system as installed in the Accelerator Lab. of ICR, Kyoto University.
Fig. 30: Schematic of the probe construction of the emittance monitor.
Fig. 31: He^+ and N^{2+} ion beam transmissions in the RFQ as a function of rf power. The measurements of F3 represent a total un-analyzed current of a beam that comes out of the RFQ.
Fig. 32: The measured input and output emittance data of a He^+ beam as superposed on the results of calculations.
Fig. 33: Measured momentum spectra of He^+, N^{2+}, and C^+ accelerated ion beams as analyzed with the 15 degree bending magnet system.
Fig. 34: The measured energy spectra of C^+ beam for the varied rf power input to the RFQ
Fig. 35: The calculated energy spectra of C^+ beam by PARMTEQ for the varied rf power input to the RFQ. The rf power of 31.7 kW corresponds to VFAC=1.0.
Fig. 36: SIMS analysis of N^{2+} beam as implanted into a N-type silicon wafer of orientation (100). The angle of implantation is 0°. The expected N^{2+} beam energy is 1.17 MeV.

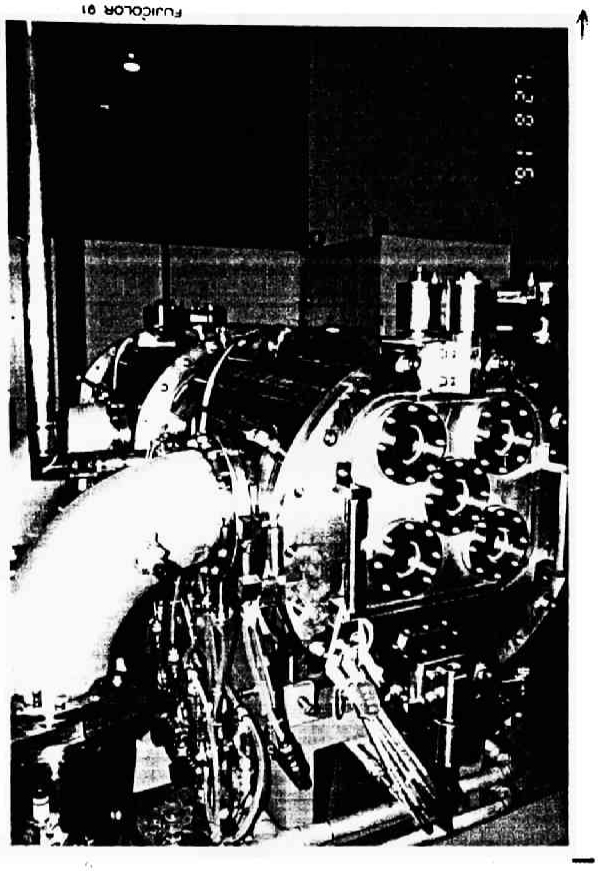

Fig. 6

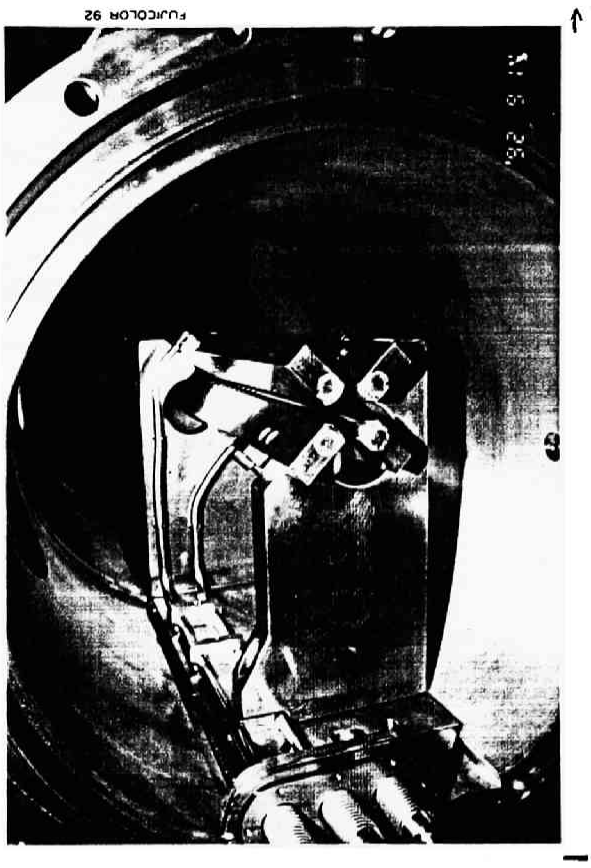

Fig. 7

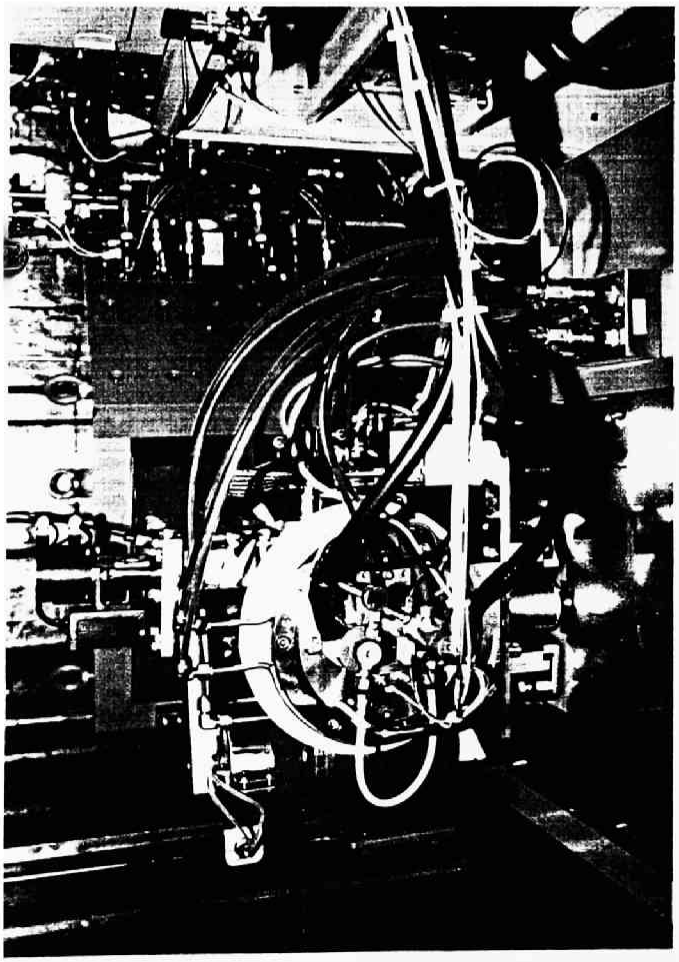

Fig. 12

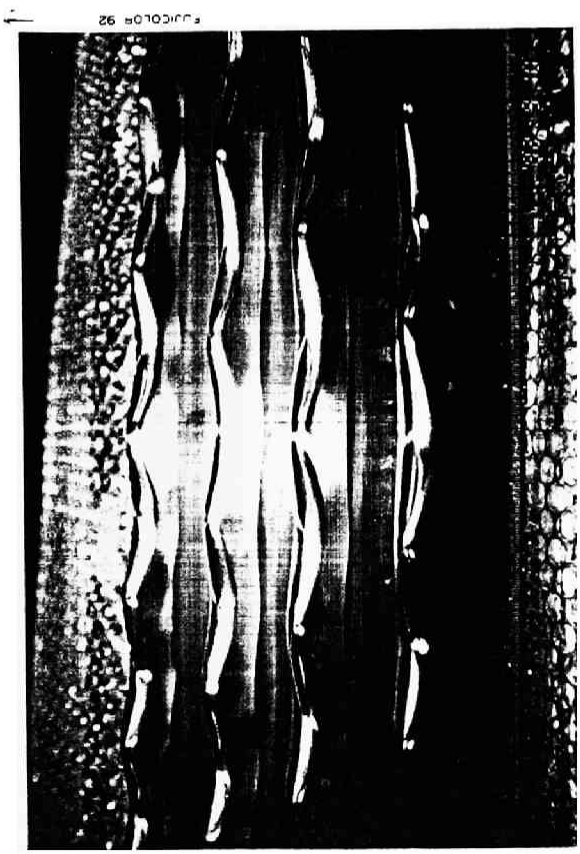

Fig. 8

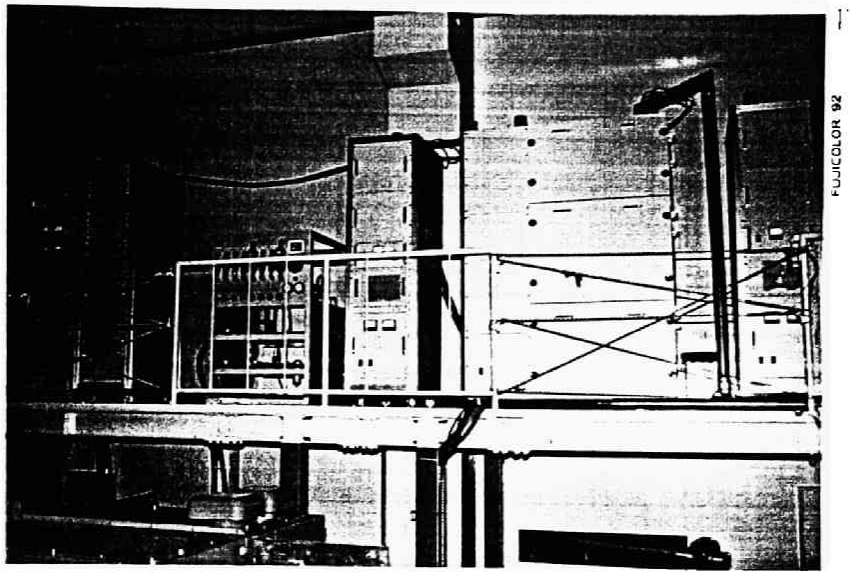

Fig. 18

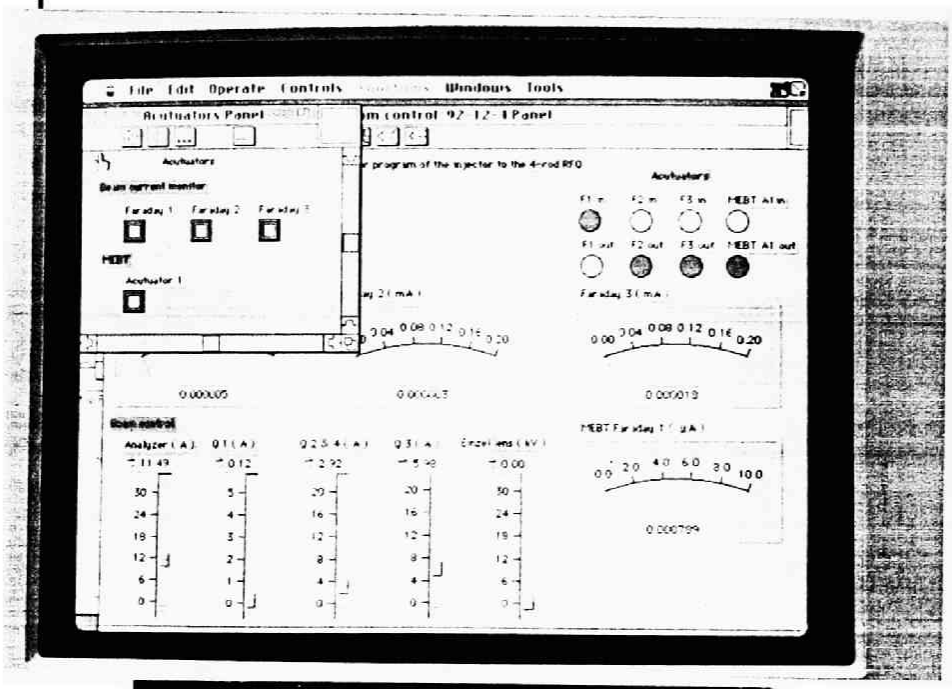

Fig. 20

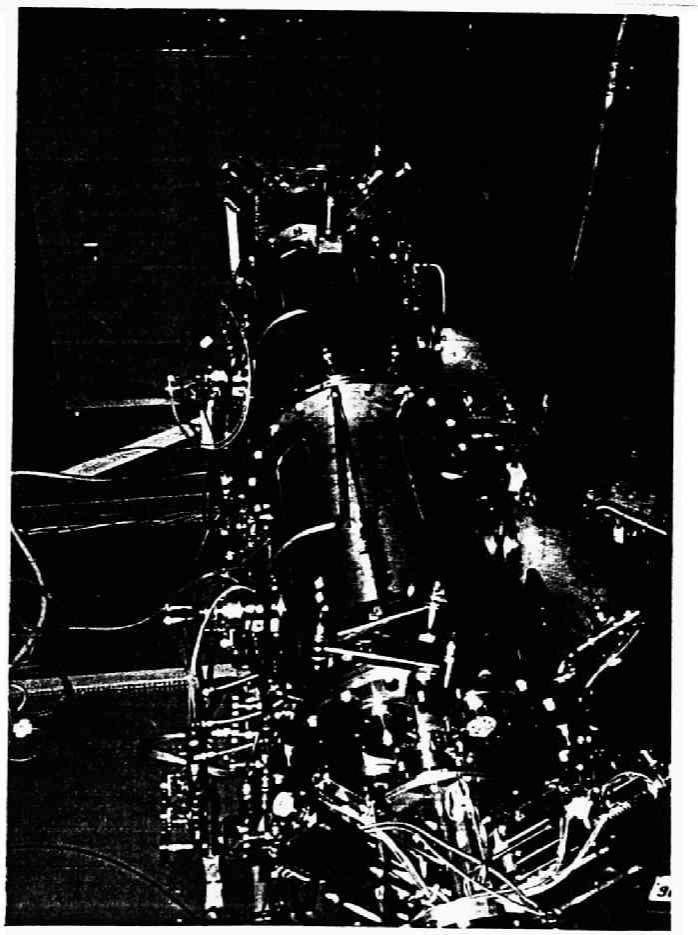

Fig. 29

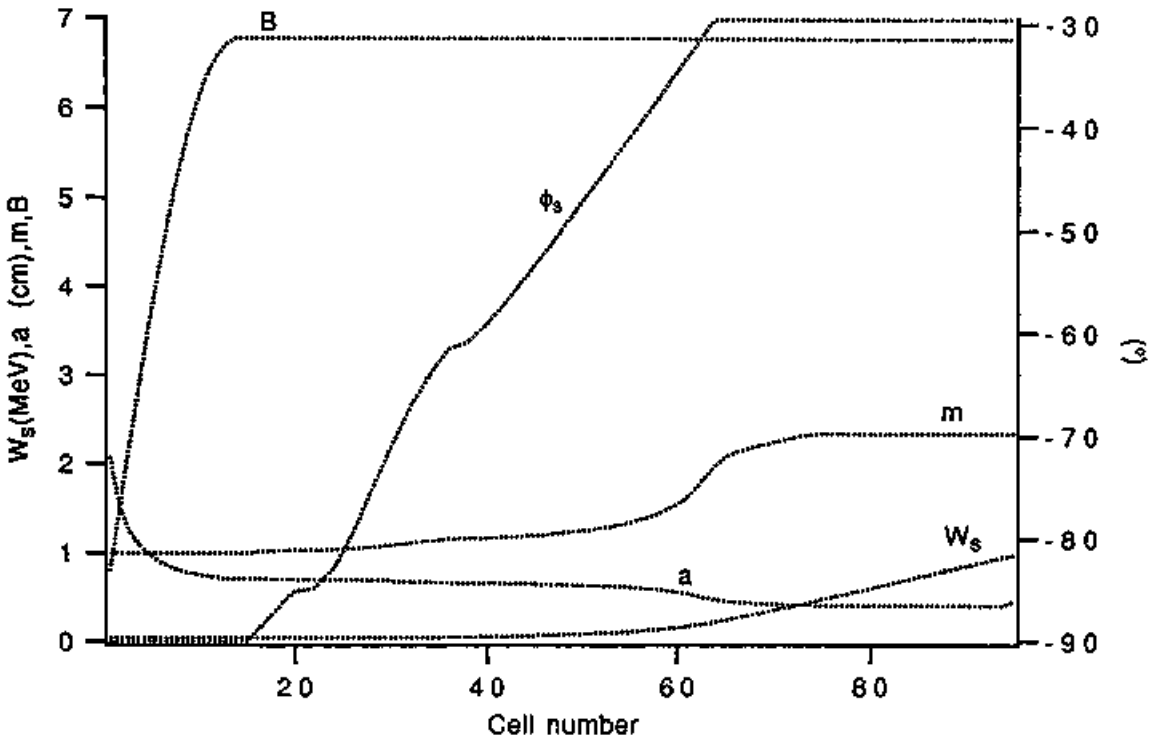
B
ϕ_s
m
W_s
a
W_s(MeV),a (cm),m,B
(°)
Cell number
0
1
2
3
4
5
6
7
20
40
60
80
-30
-40
-50
-60
-70
-80
-90

Fig. 1

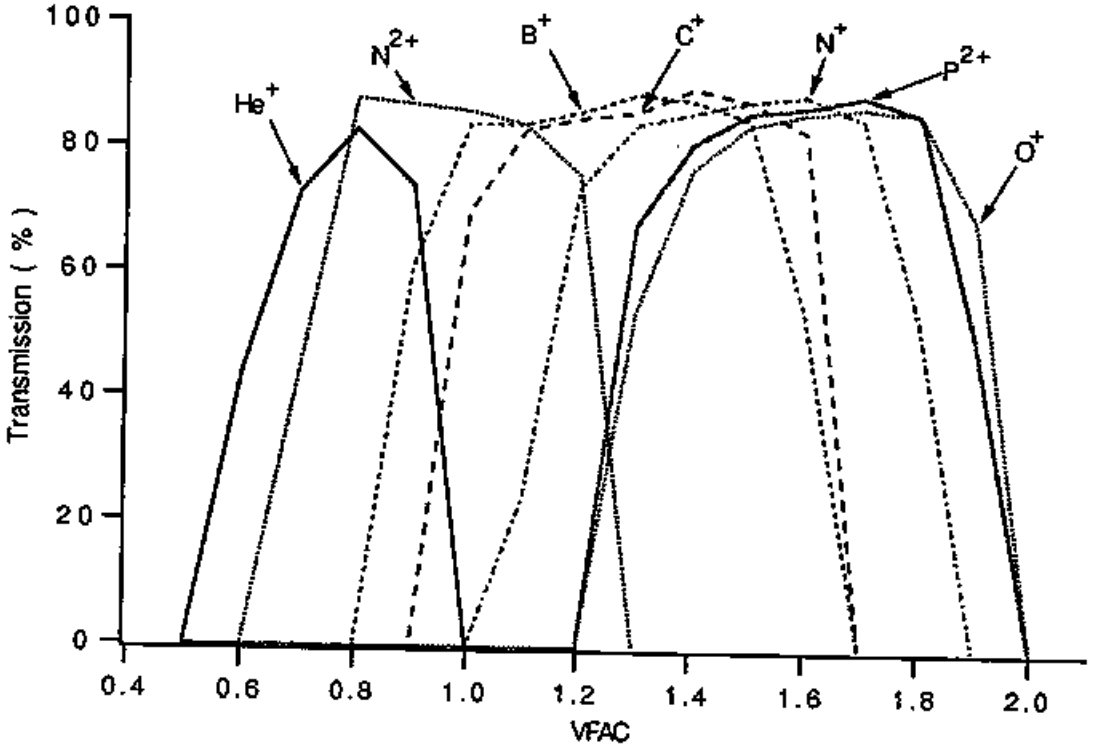
100
80
60
40
20
0
Transmission (%)
He+
N2+
B+
C+
N+
P2+
O+
0.4
0.6
0.8
1.0
1.2
1.4
1.6
1.8
2.0
VFAC

Fig. 2

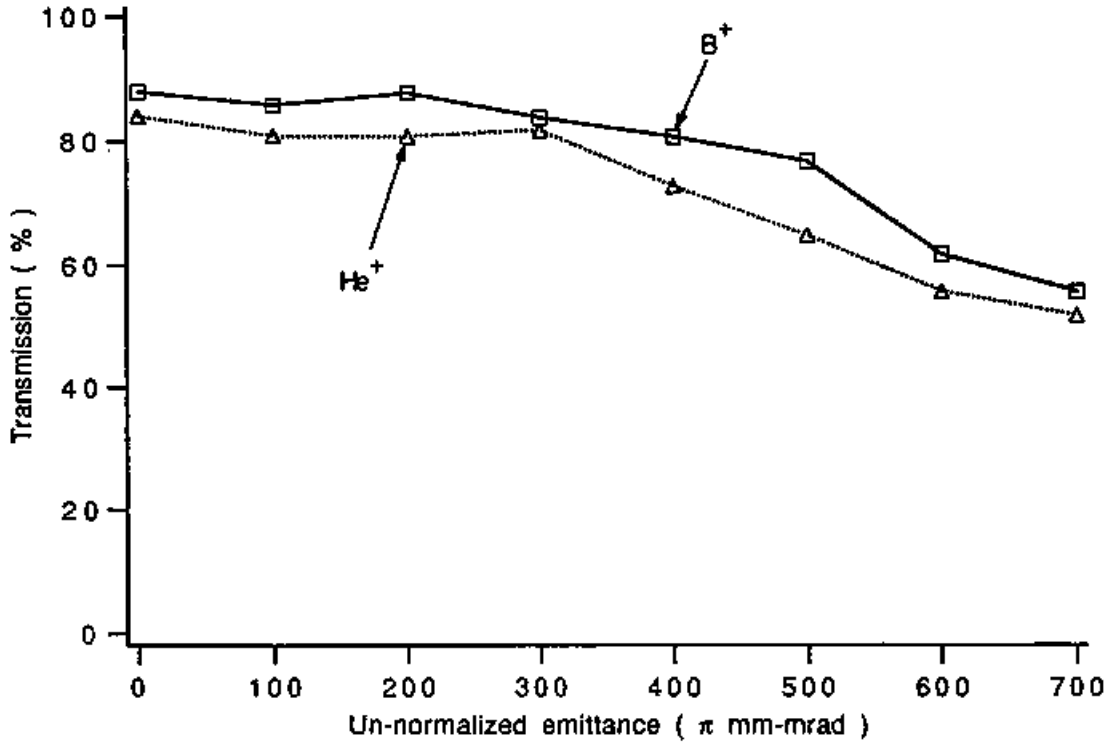
100
80
60
40
20
0
Transmission (%)
B+
He+
0
100
200
300
400
500
600
700
Un-normalized emittance (π mm-mrad)

Fig. 3

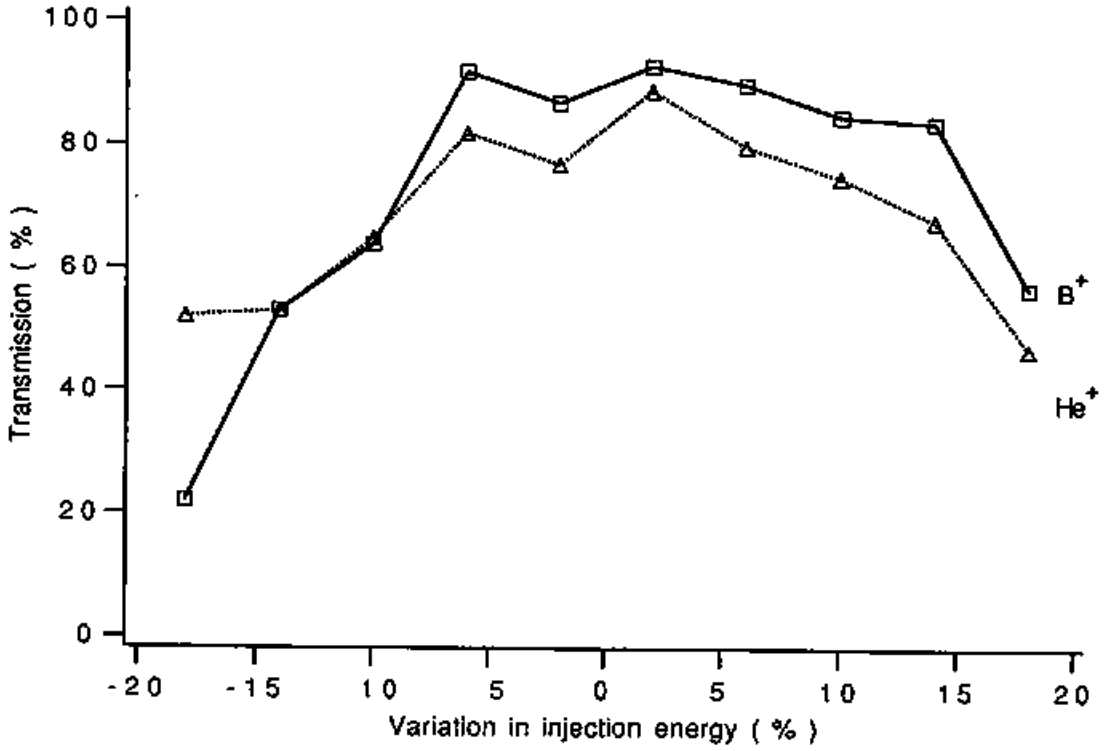
100
80
60
40
20
0
Transmission (%)
-20
-15
10
5
0
5
10
15
20
Variation in injection energy (%)
B+
He+

Fig. 4

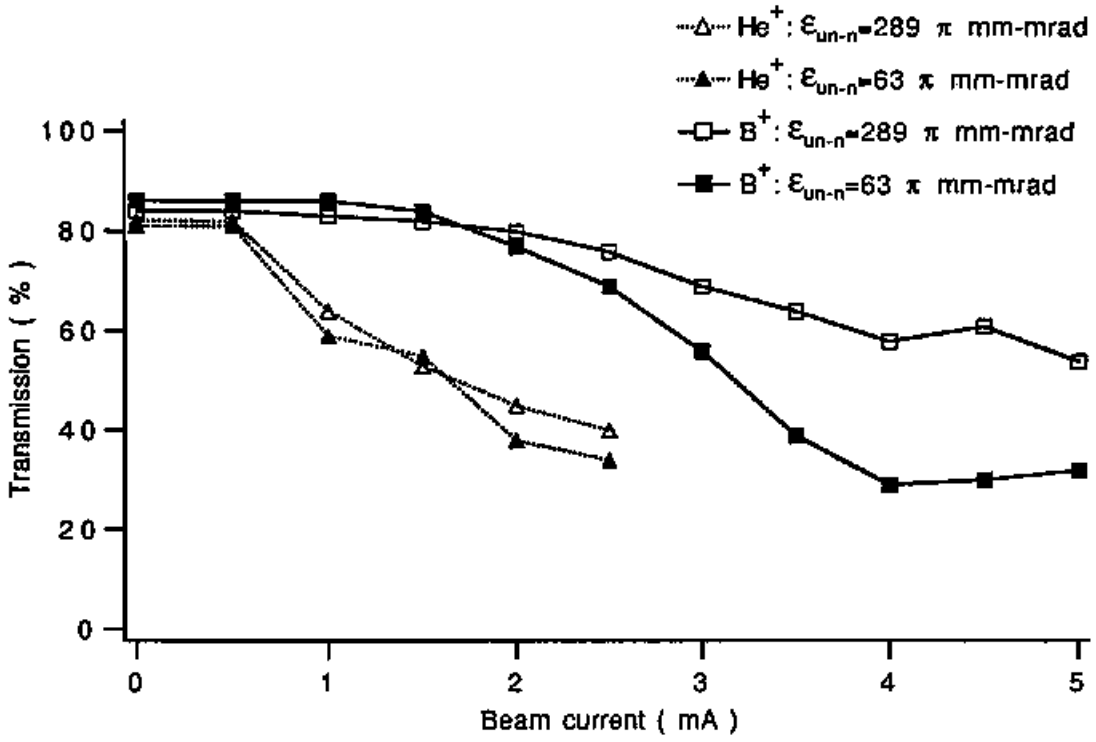
He^+: ε_{un-n}=289 π mm-mrad
He^+: ε_{un-n}=63 π mm-mrad
B^+: ε_{un-n}=289 π mm-mrad
B^+: ε_{un-n}=63 π mm-mrad
Transmission (%)
100
80
60
40
20
0
0
1
2
3
4
5
Beam current (mA)

Fig. 5

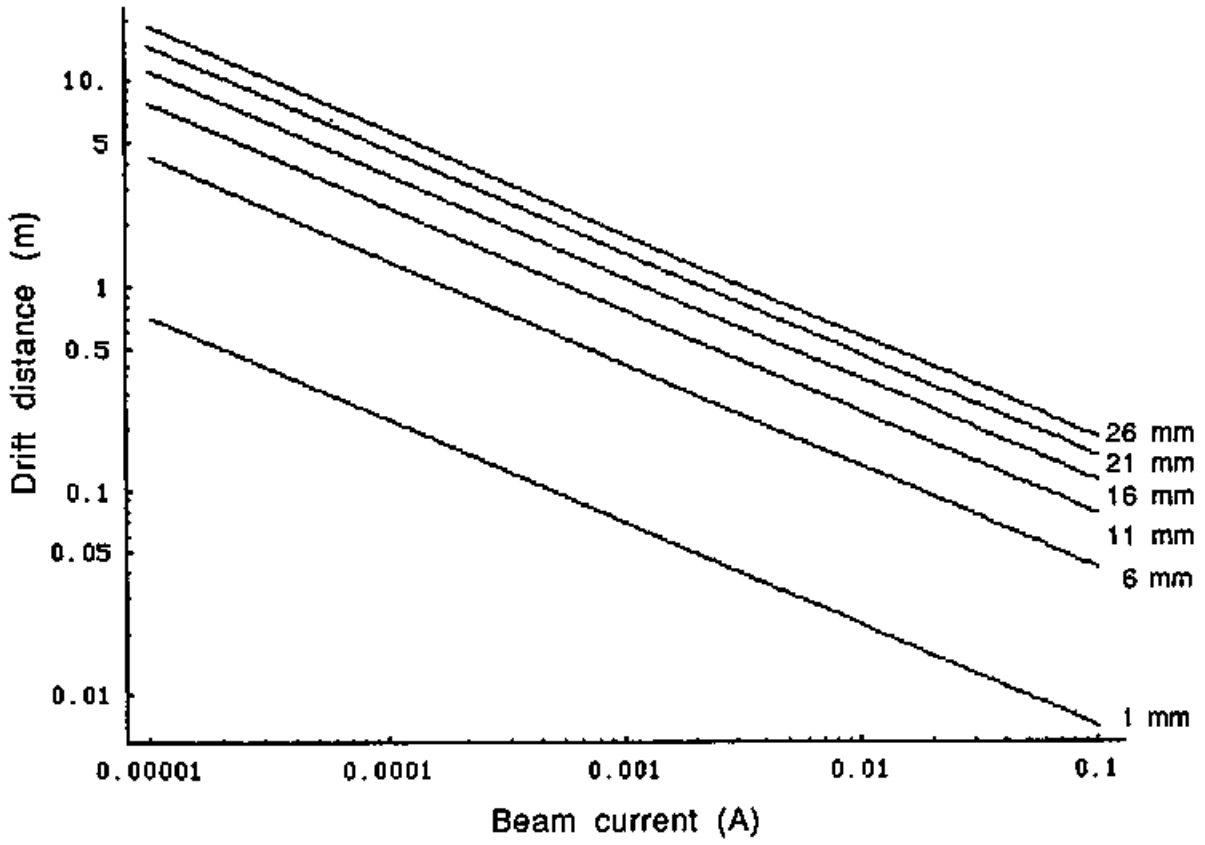
Drift distance (m)
10.
5
1
0.5
0.1
0.05
0.01
0.00001
0.0001
0.001
0.01
0.1
Beam current (A)
26 mm
21 mm
16 mm
11 mm
6 mm
1 mm

Fig. 9

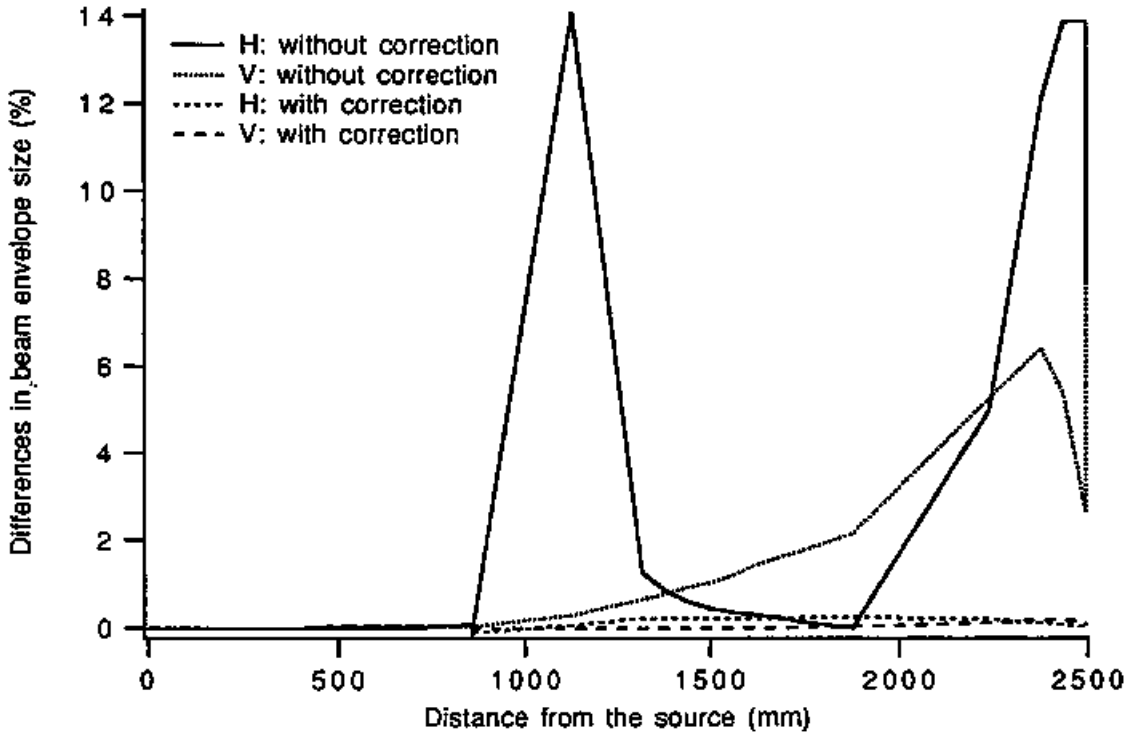
H: without correction
V: without correction
H: with correction
V: with correction
Differences in beam envelope size (%)
0
2
4
6
8
10
12
14
0
500
1000
1500
2000
2500
Distance from the source (mm)

Fig. 10

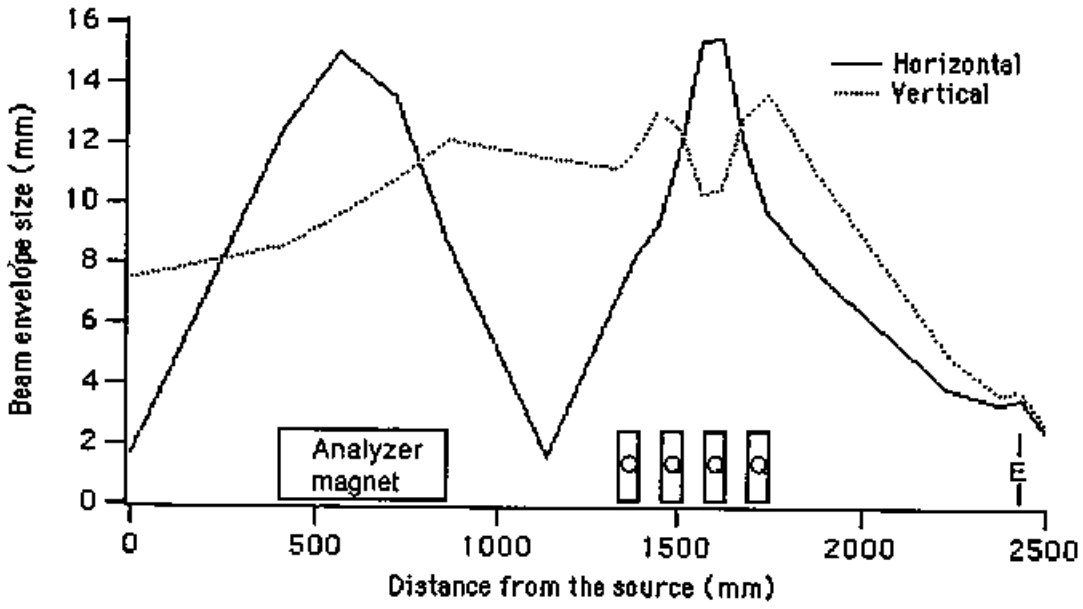
Beam envelope size (mm)
16
14
12
10
8
6
4
2
0
Horizontal
Vertical
Analyzer magnet
Q
Q
Q
Q
E
0
500
1000
1500
2000
2500
Distance from the source (mm)

Fig. 11

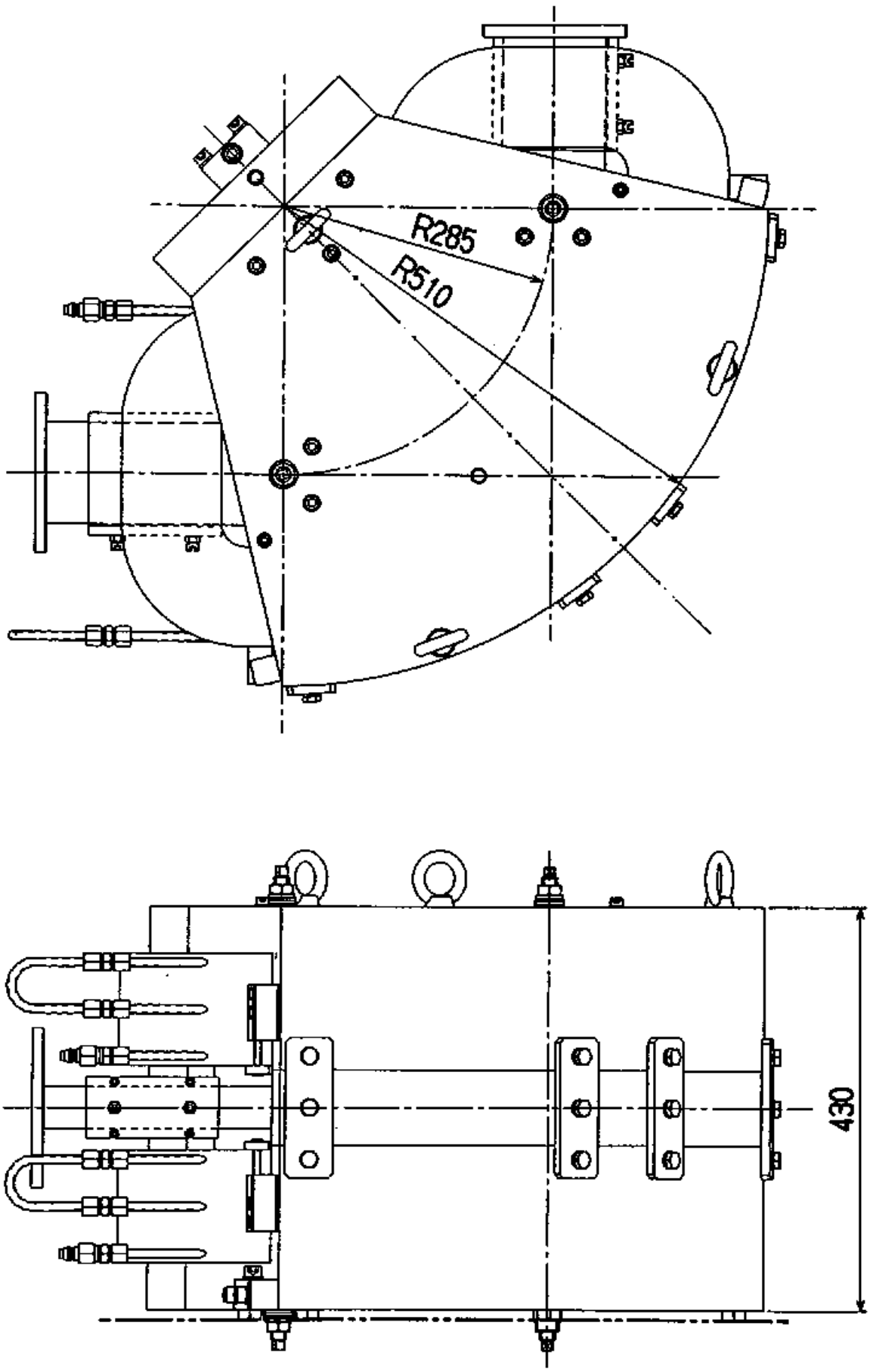

Fig. 13

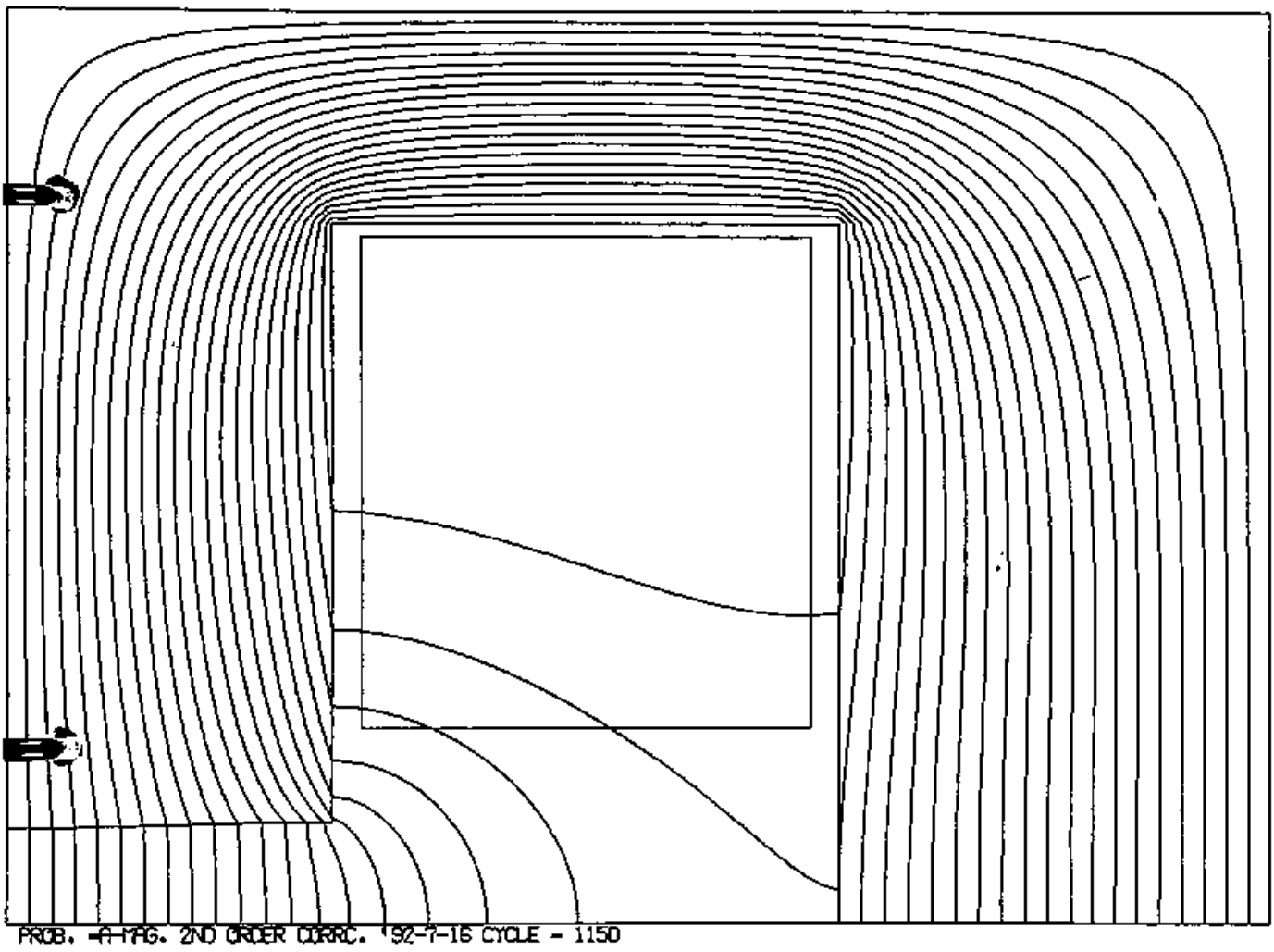

Fig. 14

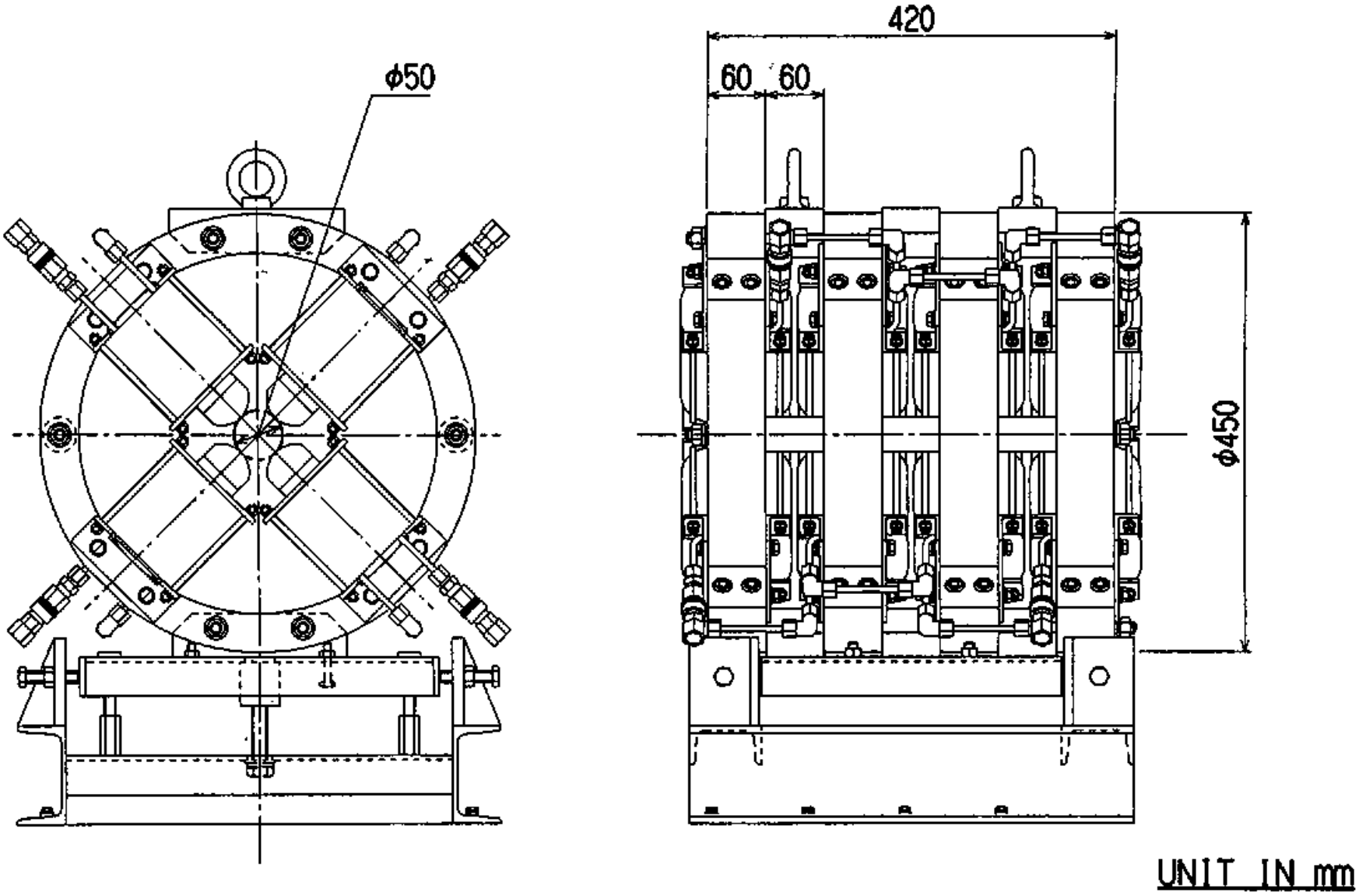

Fig. 15

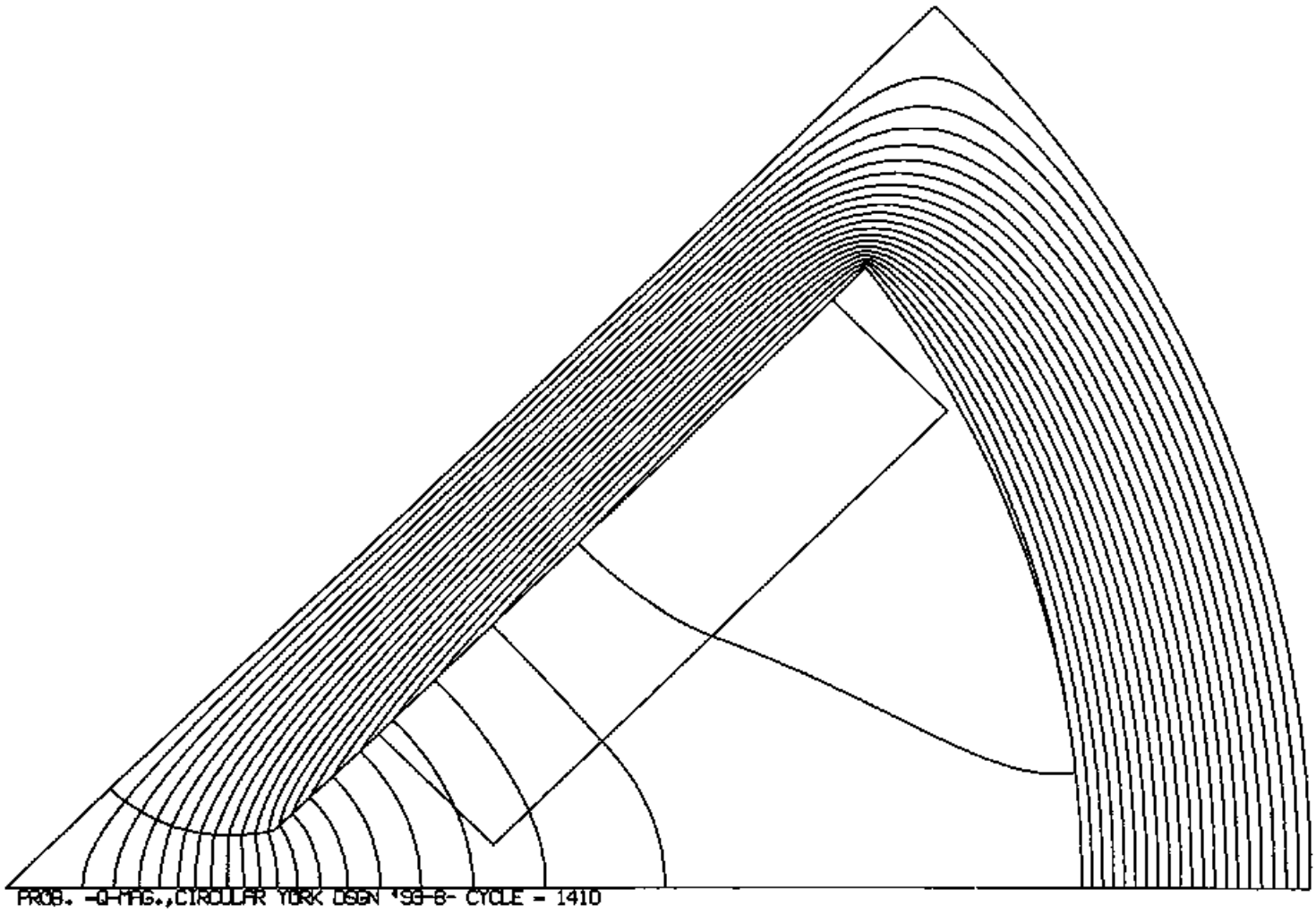

Fig. 16

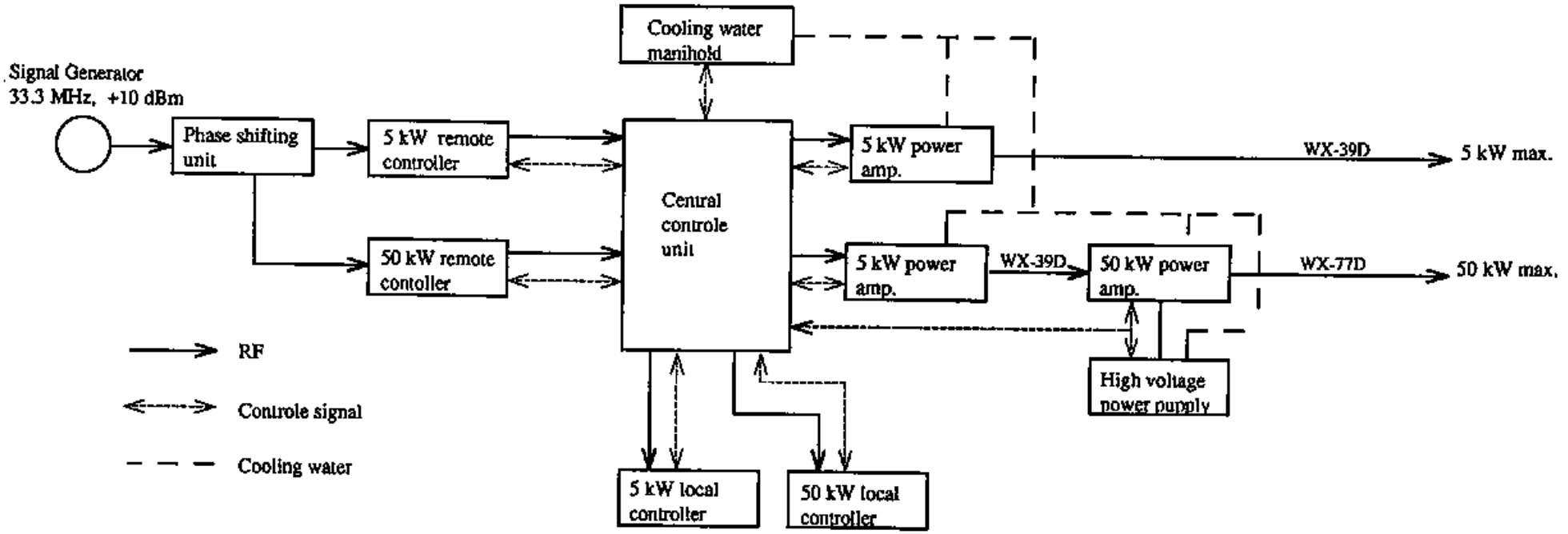
Signal Generator
33.3 MHz, +10 dBm
Phase shifting unit
5 kW remote controller
50 kW remote contoller
Cooling water manihold
Central controle unit
5 kW power amp.
WX-39D
5 kW max.
5 kW power amp.
WX-39D
50 kW power amp.
WX-77D
50 kW max.
High voltage power pupply
5 kW local controller
50 kW local controller
RF
Controle signal
Cooling water

Fig. 17

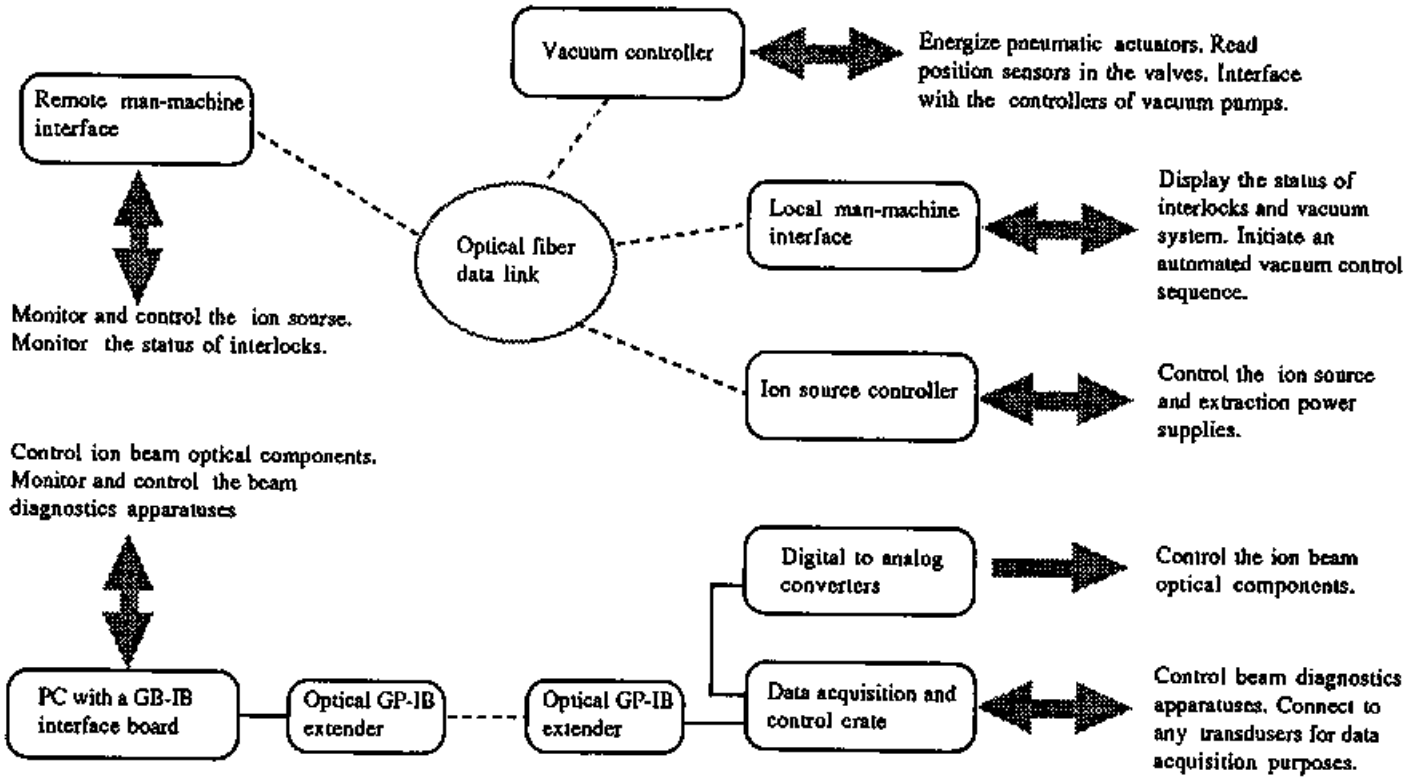
Vacuum controller
Energize pneumatic actuators. Read position sensors in the valves. Interface with the controllers of vacuum pumps.
Remote man-machine interface
Optical fiber data link
Local man-machine interface
Display the status of interlocks and vacuum system. Initiate an automated vacuum control sequence.
Monitor and control the ion source.
Monitor the status of interlocks.
Ion source controller
Control the ion source and extraction power supplies.
Control ion beam optical components.
Monitor and control the beam diagnostics apparatuses
Digital to analog converters
Control the ion beam optical components.
PC with a GB-IB interface board
Optical GP-IB extender
Optical GP-IB extender
Data acquisition and control crate
Control beam diagnostics apparatuses. Connect to any transdusers for data acquisition purposes.

Fig. 19

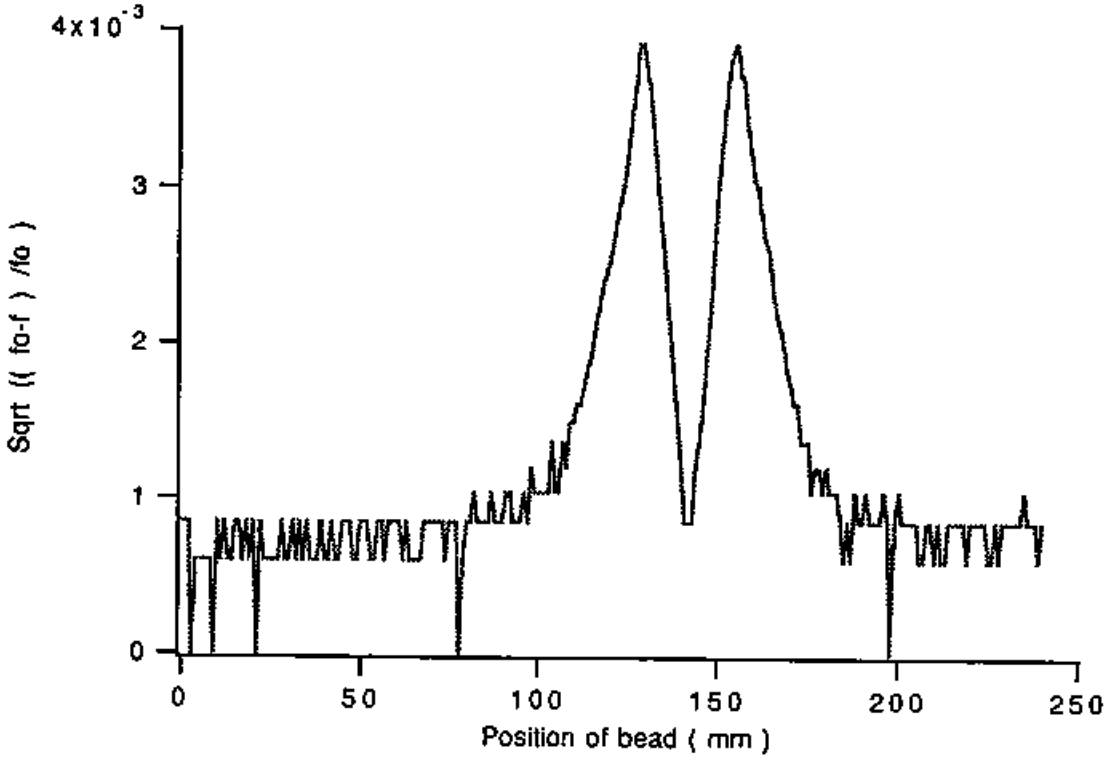

Fig. 21

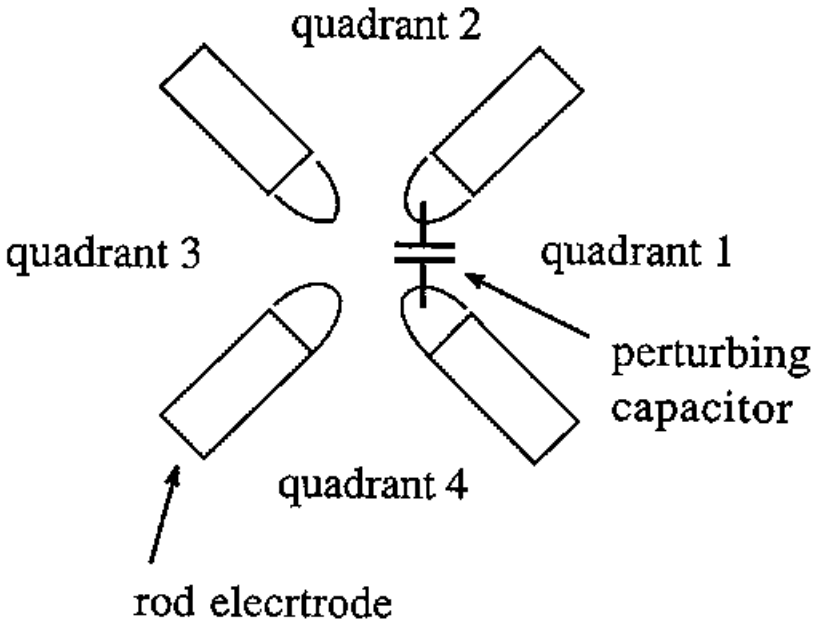
quadrant 2
quadrant 3
quadrant 1
perturbing
capacitor
quadrant 4
rod elecrtrode

Fig. 22

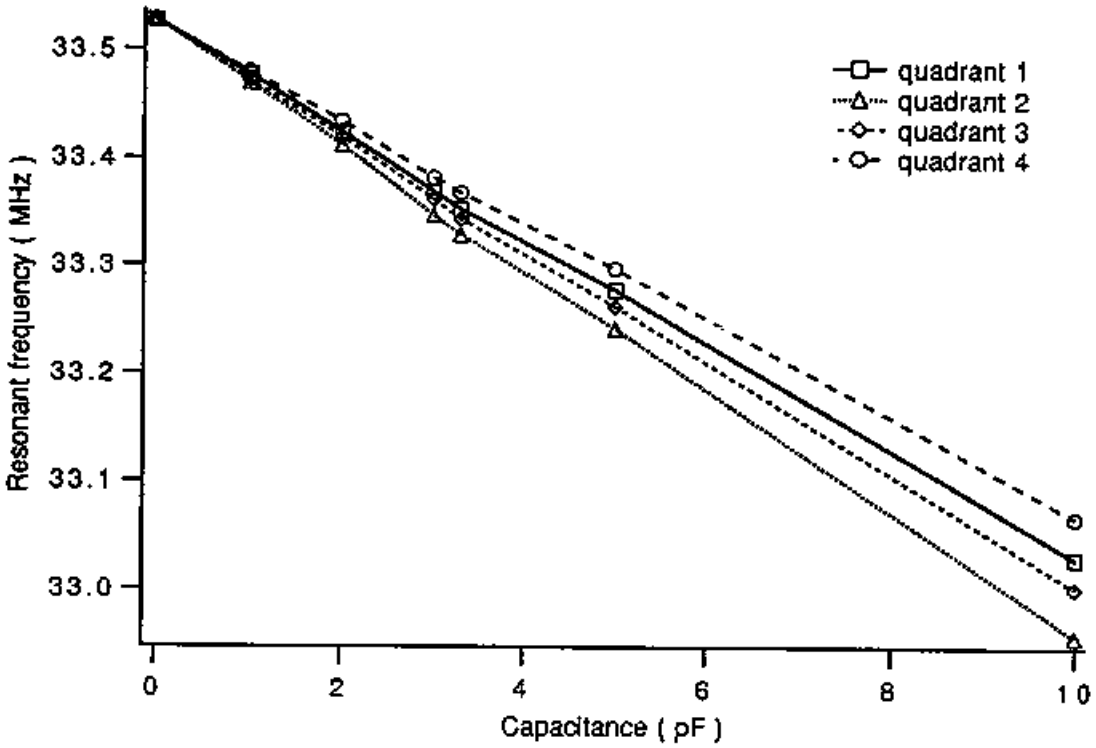
quadrant 1
quadrant 2
quadrant 3
quadrant 4
Resonant frequency (MHz)
33.5
33.4
33.3
33.2
33.1
33.0
0
2
4
6
8
10
Capacitance (pF)

Fig. 23

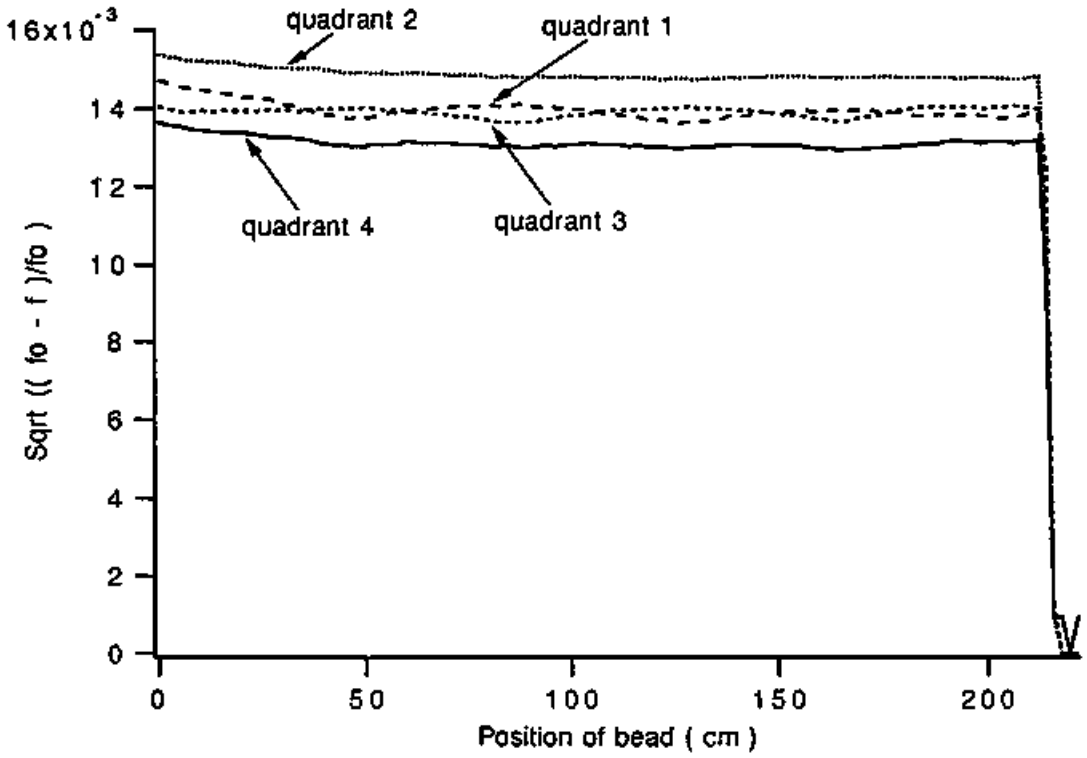
16x10^-3
14
12
10
8
6
4
2
0
Sqrt ((fo - f)/fo)
quadrant 2
quadrant 1
quadrant 4
quadrant 3
0
50
100
150
200
Position of bead (cm)

Fig. 24

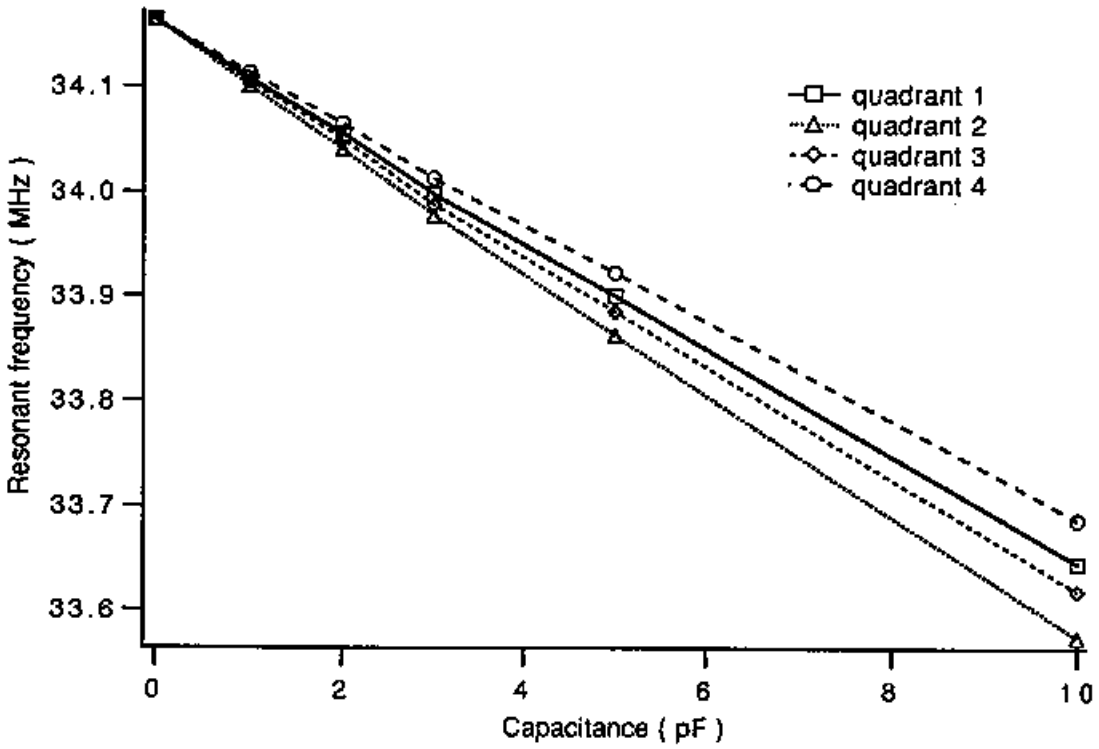
quadrant 1
quadrant 2
quadrant 3
quadrant 4
Resonant frequency (MHz)
34.1
34.0
33.9
33.8
33.7
33.6
0
2
4
6
8
10
Capacitance (pF)

Fig. 25

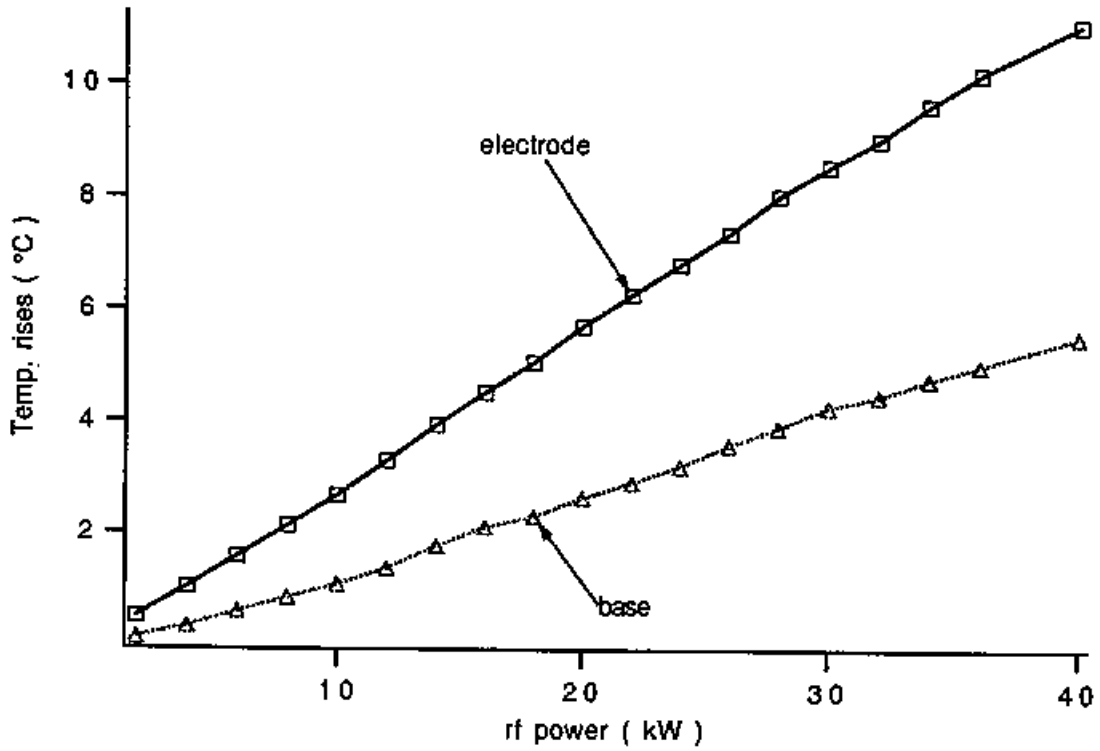

Fig. 26

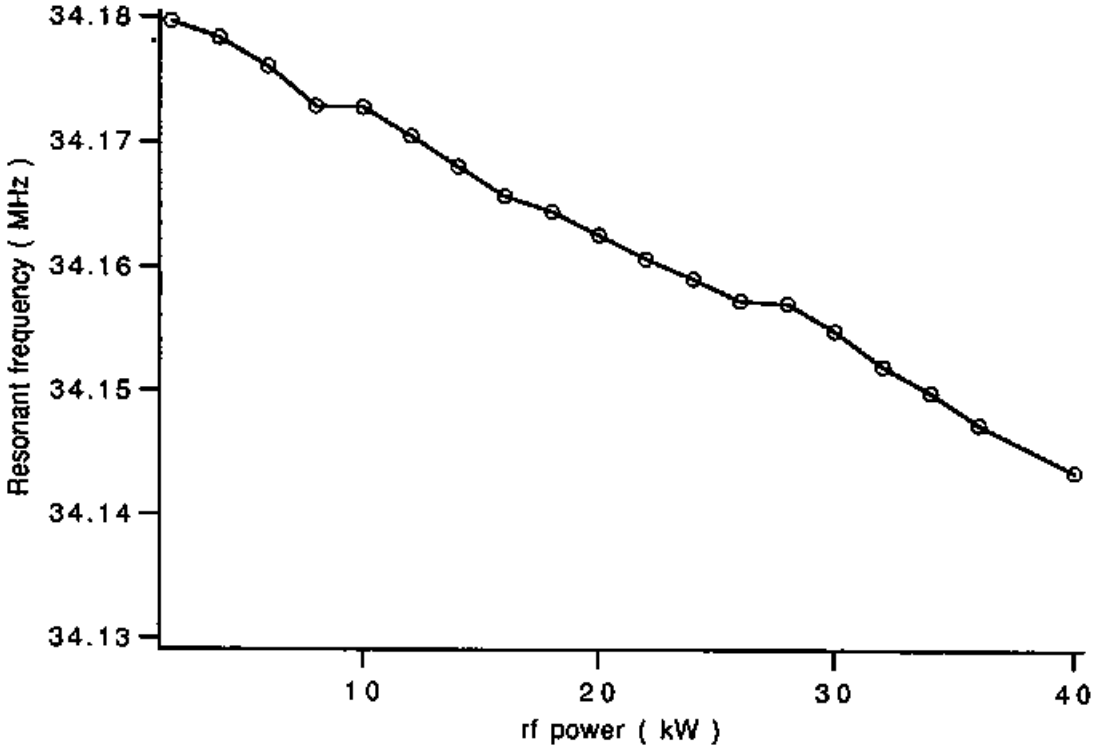
34.18
34.17
34.16
34.15
34.14
34.13
Resonant frequency (MHz)
10
20
30
40
rf power (kW)

Fig. 27

Descriptions of icons

Fixed Faraday.

Retractable Faraday.

Gate valve.

Beam defining slit.

Emittance monitor.

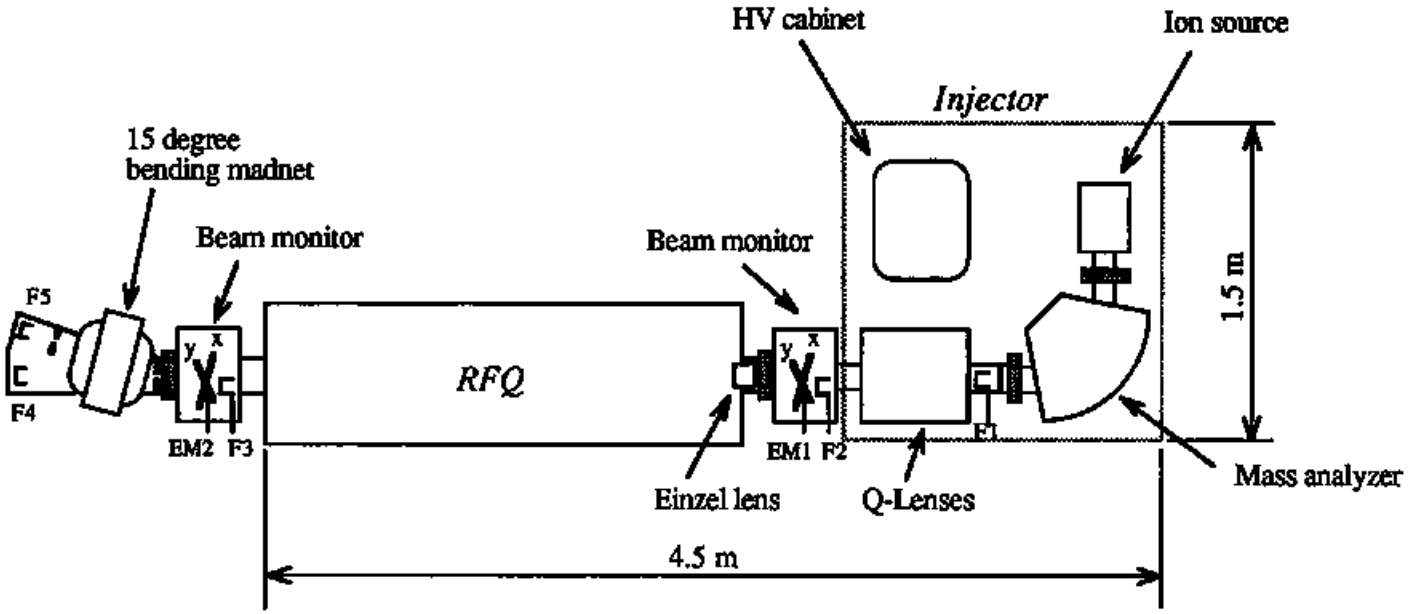

Fig.28

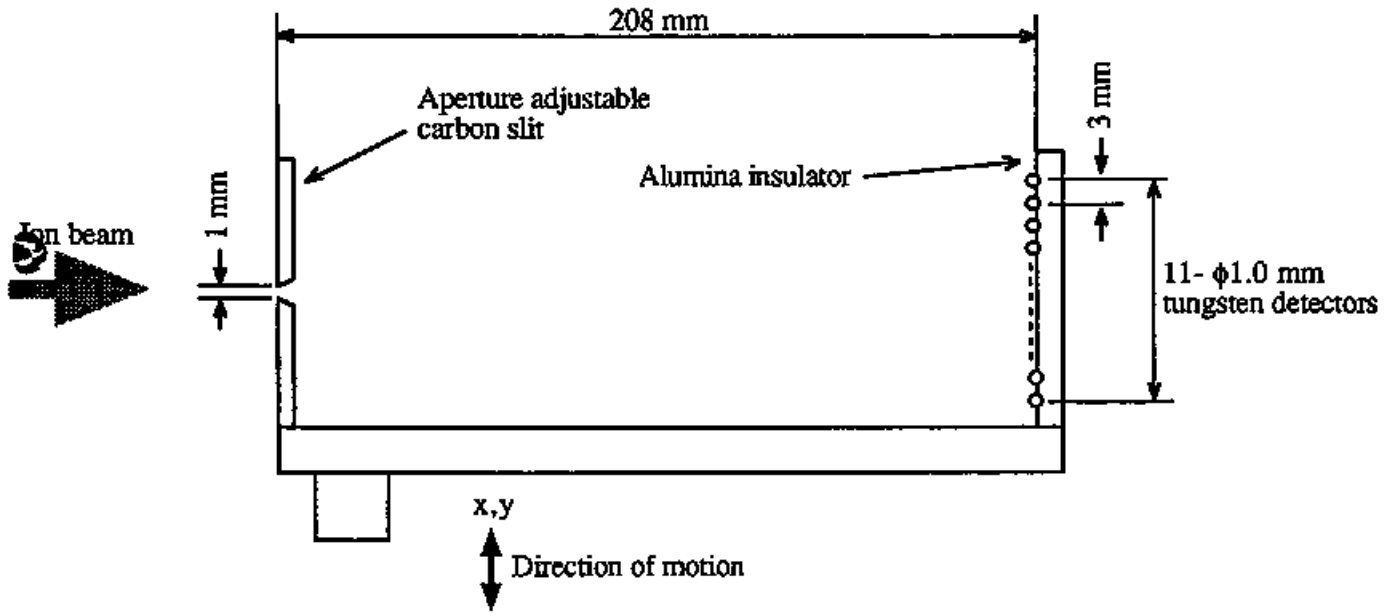
208 mm
Aperture adjustable
carbon slit
Alumina insulator
3 mm
1 mm
Ion beam
11- ϕ1.0 mm
tungsten detectors
x,y
Direction of motion

Fig. 30

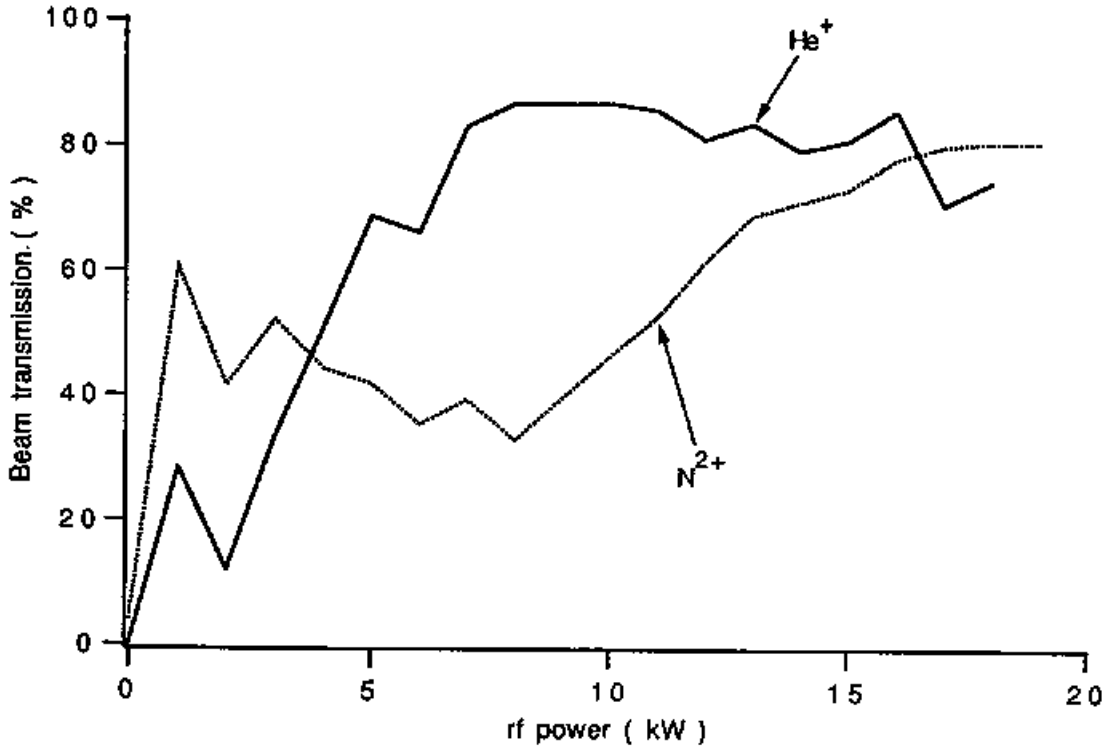

Fig. 31

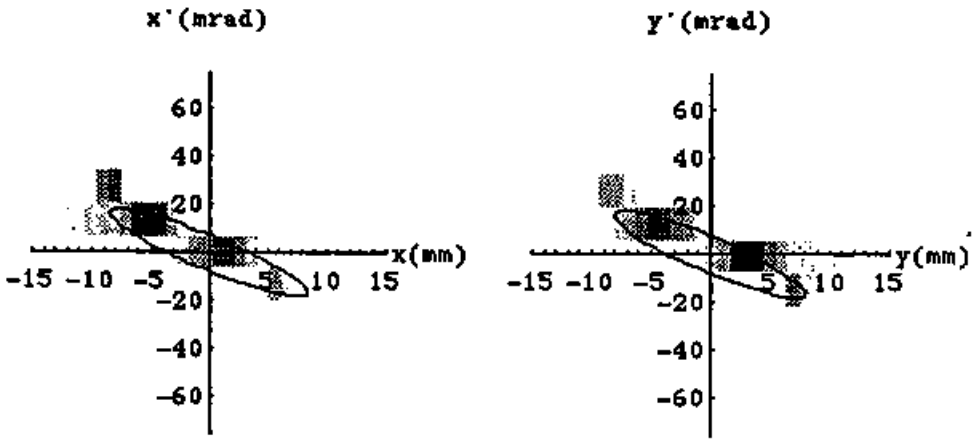

Input to the RFQ: the probe position is 233 mm(x) and 256 mm(y) upstream of the RFQ.

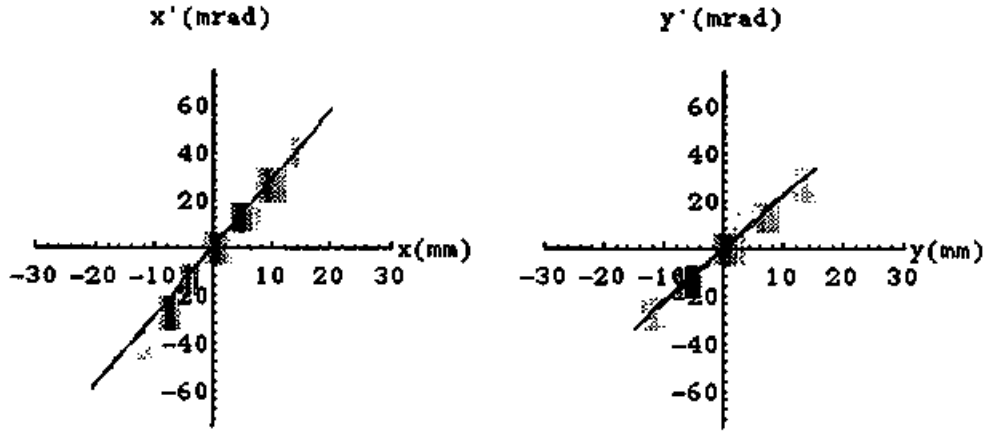

Output from the RFQ: the probe position is 388 mm(x) and 411 mm(y) downstream of the RFQ.

Fig.32

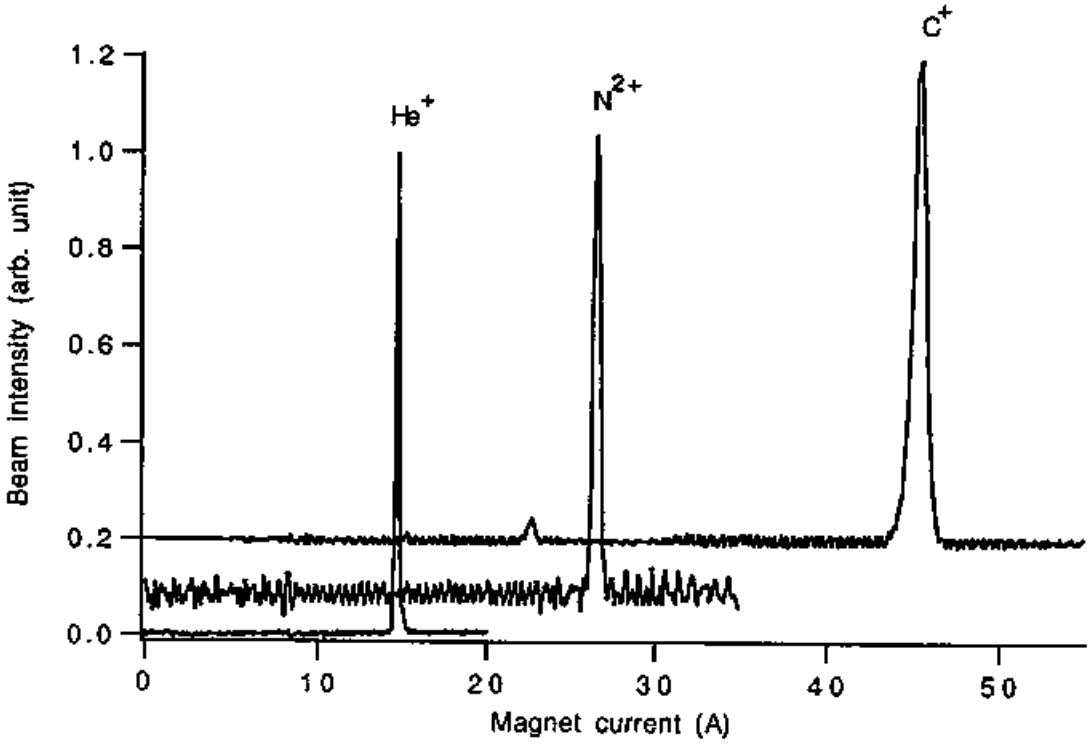
Beam intensity (arb. unit)
1.2
1.0
0.8
0.6
0.4
0.2
0.0
He+
N2+
C+
0
10
20
30
40
50
Magnet current (A)

Fig. 33

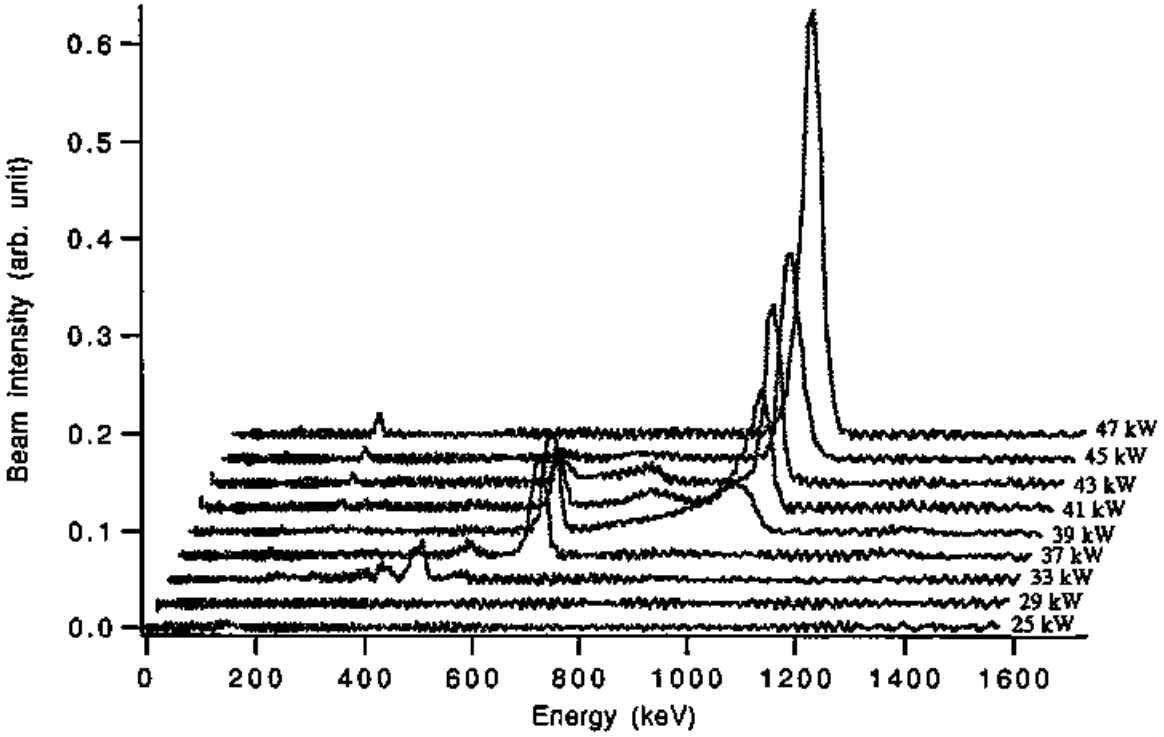
Beam intensity (arb. unit)
0.0
0.1
0.2
0.3
0.4
0.5
0.6
0
200
400
600
800
1000
1200
1400
1600
Energy (keV)
47 kW
45 kW
43 kW
41 kW
39 kW
37 kW
33 kW
29 kW
25 kW

Fig. 34

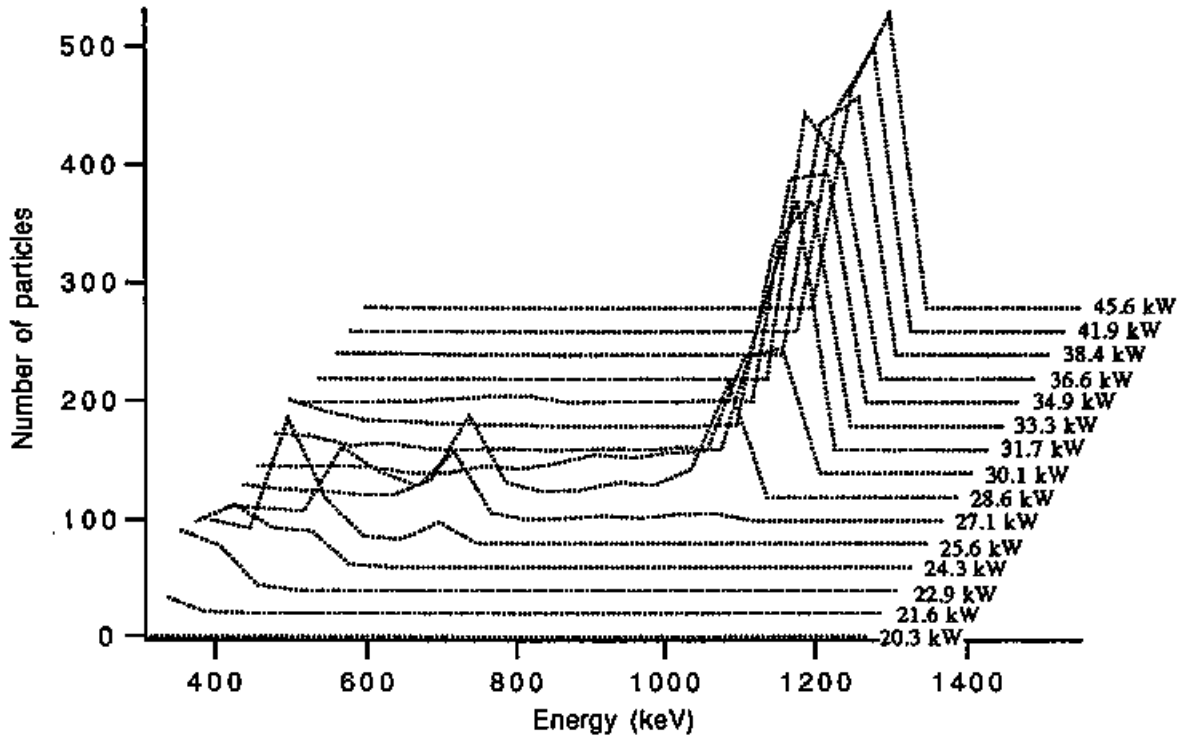
Number of particles
500
400
300
200
100
0
400
600
800
1000
1200
1400
Energy (keV)
45.6 kW
41.9 kW
38.4 kW
36.6 kW
34.9 kW
33.3 kW
31.7 kW
30.1 kW
28.6 kW
27.1 kW
25.6 kW
24.3 kW
22.9 kW
21.6 kW
20.3 kW

Fig. 35

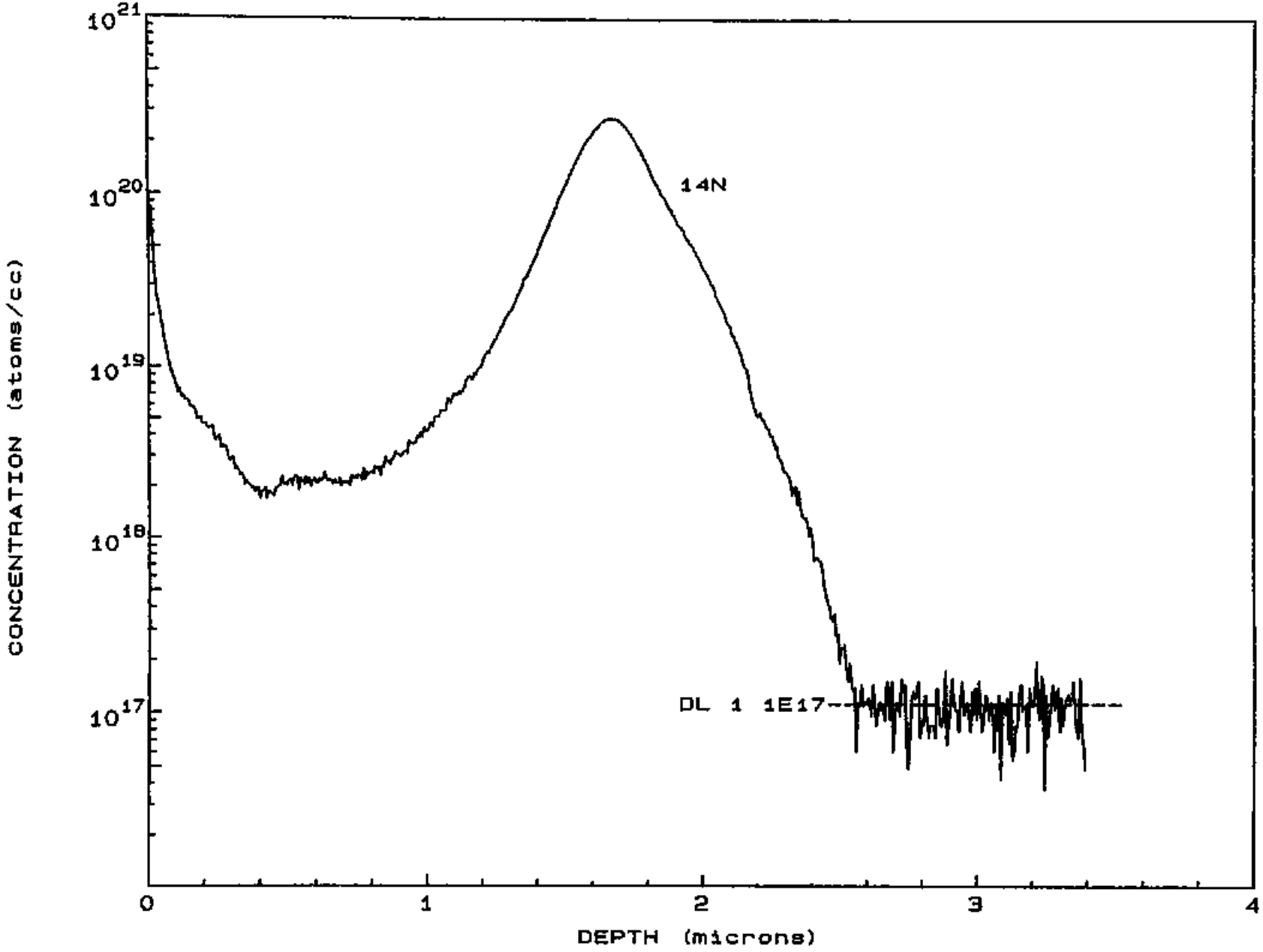
CONCENTRATION (atoms/cc)
10^{21}
10^{20}
10^{19}
10^{18}
10^{17}
14N
DL 1 1E17
0
1
2
3
4
DEPTH (microns)

Fig. 36

Table 1
The specifications of the 4-rod RFQ linac system.

Injector:		
	Ion source	Freeman type
	Extraction voltage	50 keV max.
	Mass analyzer	90° magnet with sextupole corrections
	Focusing elements	four magnetic quadrupole lenses and one Einzel lens
	Beam optical length	2.5 m, including a beam monitor
	Size	1.5(W)×1.5(D)×1.8(H)
RFQ:		
	Type	fixed frequency "modified" 4-rod
	Frequency	33.3 MHz (design)
	Diameter	60 cm i.d., 67 cm o.d.
	Length	2.3 m
	rf power	50 kW max.
	Operation mode	c w
Overall performances:		
	Ion species	≥1/16 in charge to mass ratio
	Current	200 μA, nominal
	Energy	83.5 keV/u (919 keV for B^+)
	Transmission	≥80 %

Table 2
Key design parameters of the 4-rod RFQ.

Frequency	33.3 MHz
Average bore radius	0.8 cm
Focusing strength	6.79
Inter-electrode voltage	54.9 kV
Charge to mass ratio	1/11
Injection energy	2.73 keV/u
Output energy	83.5 keV/u
Length of electrode	222 cm
Cavity inner diameter	60 cm

Table 3
Comparisons of the first order and second order calculations in the LEBT section of the beam line. The sextupole corrections made in the analyzing magnet are very effective in obtaining a quality beam at the RFQ entrance.

	Horizontal	Vertical
Beam parameters at the source:		
Emittance (π mm mrad)	50	75
α (unit less)	0.0	0.0
β (mm/mrad)	0.0558	0.75
1/2 beam size (mm)	1.67	7.5
1/2 beam divergence (mrad)	30	10

	1st order	2nd order w/o correction	2nd order with correction
Beam parameters at the RFQ entrance:			
Horizontal			
1/2 beam size (mm)	2.62	2.83 (0.995)	2.62 (-0.004)
1/2 beam div. (mrad)	27 4	29.3 (-7.16)	27.5 (-0.816)
Vertical			
1/2 beam size (mm)	2.62	2.83 (-0.995)	2.62 (0.004)
1/2 beam div. (mrad)	27.4	29.3 (7.16)	27.5 (0.816)

Note: Numbers in parenthesis are shifts of beam centroids.

Table 4
The rf characteristics of 4-rod RFQ with the copper un-modulated electrodes and aluminum posts.

	c.v. method	bead pull	network
f_o	------	------	33.5275 MHz
Q_o	------	------	5000
R_o/Q_o	14.4 Ω	18.9 Ω	------
R_o	72.0 kΩ	94.5 kΩ	------
rf power	20.9 kW	15.9 kW	------
field balance	+6,-5 %	±6 %	------

Table 5
The rf characteristics of 4-rod RFQ with the copper modulated electrodes and copper posts.

	c.v. method	network
f_o	------	34.1635 MHz
Q_o	------	3300
R_o/Q_o	14.4	------
R_o	47.6 kΩ	------
rf power	31.7 kW	------
field balance	+6,-5 %	------

Table 6
Specification of the emittance monitor.

Slit width	1 mm (adjustable)
Drift distance from the slit to the detector rods	208 mm
Number of the detector rods	11
Diameter of the detector rods	1 mm
Angular separation of the detector rods	14 mrad
Spacing between the detector rods	3 mm
Maximum acceptable beam divergence	±72 mrad
Maximum range of the probe span	±20 mm
Resolution of the probe position	0.1 mm

Table 7
Typical results of the beam intensity measurments of He^+, N^{2+}, and C^+ ion beam by Faraday cups F2 and F3 The condition of beam injection is differnt in He^+ and the other two ions: the Einzel lens was used for He^+ but not used for N^{2+} and C^+ beams.

Ions	Beam currents (pμA)	Beam transmission (%)
He^+	32	86
N^{2+}	13	79
C^+	220	78